



Parametrically excited microcantilever beam under large deflection and mass sensing

Nikul Jani · G. Chakraborty · Surendra Verma

Received: 25 July 2022 / Accepted: 23 March 2023 / Published online: 14 April 2023
© Springer Nature B.V. 2023

Abstract Dynamic analysis of feedback-based parametric instability in microcantilever beam with the consideration of microsize effect has been carried out. The effect of nonlinearities caused by large deflection and feedback has also been considered. Multiple scales scheme has been utilized for the study, and the outcomes have been verified using generalized differential quadrature method and Galerkin approach. Parametric instability has been realized as a valuable phenomenon for mass detection. Here, a method of mass sensing has been presented, which is based on determining the change in the amplitude. The method has been demonstrated through parametric resonance in the first and second modes. Sensitivity of the proposed technique is compared with the sensitivity values of some of the MEMS resonator-based mass sensing devices. It is found that the proposed method can provide better sensitivity even while using a comparatively larger size microbeam. The strategy can

provide robust performance in the presence of significant damping, too.

Keywords Microcantilever beam · Mass sensor · Parametric excitation · Feedback · Nonlinearities · Microsize effect

List of symbols

A	Area of the beam section
α_c	Coefficient of sensor/feedback nonlinearity
C_d	Damping coefficient
G_d	Gain of direct excitation
G	Gain of parametric excitation
I	Second moment of area
α_g	Geometric nonlinearity coefficient
α_i	Inertial nonlinearity coefficient
L	Length of beam
l_s	Length-scale parameter
α	Nondimensionalized coefficient of sensor nonlinearity
ν	Nondimensionalized damping coefficient
$\delta\nu$	Sensor output
S_n	Sensitivity for mass sensing based on amplitude change for nondimensionalized beam
$(S_n)_a$	Sensitivity for mass sensing based on amplitude change
μ	Shear modulus
d	Thickness of beam
b	Width of beam
E	Young's modulus

N. Jani (✉) · G. Chakraborty
System Dynamics and Control Laboratory, Department
of Mechanical Engineering, Indian Institute of Technology
Kharagpur, Kharagpur, West Bengal 721302, India
e-mail: nikul.jani28@gmail.com

G. Chakraborty
e-mail: goutam@mech.iitkgp.ac.in

S. Verma
Department of Aerospace Engineering, Indian
Institute of Technology Kharagpur, Kharagpur,
West Bengal 721302, India
e-mail: surendraverma2501@gmail.com

1 Introduction

Among the different Microelectromechanical systems (MEMS) based technologies, microresonator-based devices have become a domain of significant interest. In resonant MEMS, microstructures are deliberately driven to resonance to derive certain benefits, for example, for sensing of very small forces [1], fluid flow [2], pressure [3], motion [4], etc. Resonance-based mass sensing has shown superior performance over static mode sensing [5]. Among micro-nano resonant mass sensing devices, resonance characteristics of microstructures with and without added mass are studied and compared for calculating the mass value. Addition of mass causes change in the natural frequency, and detecting the change, added mass can be determined very accurately. It is possible to carry out real-time mass detection through tracking the natural frequency [6], or one can go for the hassle-free frequency sweep also. One can see plenty of examples in which MEMS resonators have been used for mass detection [7].

Below the umbrella of resonant mass sensing, detection techniques can be broadly classified on the basis of resonant behavior, whether it is linear or nonlinear. There are several examples of resonant MEMS-based mass sensors in which nonlinear characteristics have been found helpful [8, 9]. Nonlinear dynamics of MEMS resonators is also a rich field. Multiple sources cause the response of the microresonator to be nonlinear [10, 11]. Large deflection of microstructures has been a major cause of nonlinearities. For example, in the case of doubly clamped beam, the large oscillation causes stretching of the neutral axis, and it induces stiffening within doubly clamped beam [12]. In the case of a cantilever beam, vibration with large amplitude causes strong coupling of transverse and axial displacements, which induces geometric, as well as inertial nonlinearities [13].

Parametrically excited microresonators with nonlinear behavior have also been utilized for better performance in several MEMS devices [14, 15]. Parametric amplification of Coriolis force through modal coupling provides superior sensitivity and broad driving range for MEMS gyroscope [16]. Different transduction mechanisms are available at the micro/nanoscale to drive the structure to parametric resonance. Electrostatic and piezoelectric actuation techniques are the well-known excitation strategies used

for this purpose [17, 18]. To induce parametric instability through boundary conditions, harmonic motion at a certain frequency is supplied to the clamped ends of the microbeam in the axial direction. That induces inertial force in the axial direction for modulation of stiffness [19]. An array of microcantilever beams also have excited parametrically using the same approach [20]. A simple method has been demonstrated at the microscale, in which parametric excitation is induced using feedback [21, 22]. In this technique, clamped end of a cantilever beam is displaced in the transverse direction. Analytical and numerical studies for the microcantilever beam model have been carried out by the authors [23, 24]. The same working model has been considered in the present work.

In the present work, the study has been extended further for the case when the microcantilever beam is excited to large oscillation through parametric excitation. Utilizing the phenomenon of parametric instability, a method of mass sensing has been presented in which the added mass can be approximated by determining the change in the amplitude of oscillation. The presented mass sensing technique has been presented before through direct excitation [25]. While utilizing the region of parametric instability, it has been realized that sensitivity can be greatly enhanced. That is due to the large slope of the amplitude-frequency curve in the region of parametric instability. Geometric and inertial nonlinearities are considered in the governing equation which arise in cantilever beam due to vibration with large amplitude. Influence of microsize on the resonance characteristics is also demonstrated using perturbation and numerical analysis.

A detailed description of the working model and excitation strategy has been presented in Sect. 2. Here, a small discussion is given on sensor and feedback nonlinearity. They induce a nonlinear relationship in the excitation. Further, mathematical modelling of microcantilever beam and perturbation analysis is given in Sect. 3. Section 4 details the procedures for numerical study, where, the generalized differential quadrature method (GDQM) and Galerkin scheme are used. Results of the perturbation analysis are compared with the results of numerical methods in Sect. 5. A very good agreement has been found between the outcomes of different techniques. Based on the phenomenon of parametric instability, a mass detection technique is also demonstrated.

2 Parametrically excited microcantilever beam model

Microcantilever beam with base excitation (also called acoustic excitation) is widely used in atomic force

Clamped end of a microcantilever beam is gripped inside a holder, and a piezo actuator transversely displaces the base. When the piezo is actuated at the natural frequency, a very small displacement given causes a large displacement of the cantilever tip, and it is measured using a detection system. That is called resonant excitation. The schematic diagram of the system is shown in Fig. 1. Representative dimensions of the microcantilever beam model, used in the experimental study are given in Table 1, [21]. If the ratio of beam thickness to material length scale parameter is less than 1.5, then the effect of microsize can significantly influence the natural frequencies of microbeam. For a group of microcantilever beam, for the dimension range of $2.94 \times 50 \times (75\text{--}250) \mu\text{m}^3$, material length scale parameter for silicon microbeam has been noted down as $0.592 \mu\text{m}$ [26, 27]. For the given dimensions of microbeam, the ratio of beam thickness to material length scale parameter is higher than 1.5, and so the microsize effect will not be dominant. However, In this article, microscale effect has been considered to analyze the effect of microsize on resonant response, if the thickness of the microbeam has been chosen smaller than $2 \mu\text{m}$.

Determining the response of microstructure accurately is essential for successful resonant sensing. For the considered type of microbeam model, optical beam deflection method (OBDM) is widely used to measure the deflection of free end [28, 29]. In this

Table 1 Dimensions and material parameters

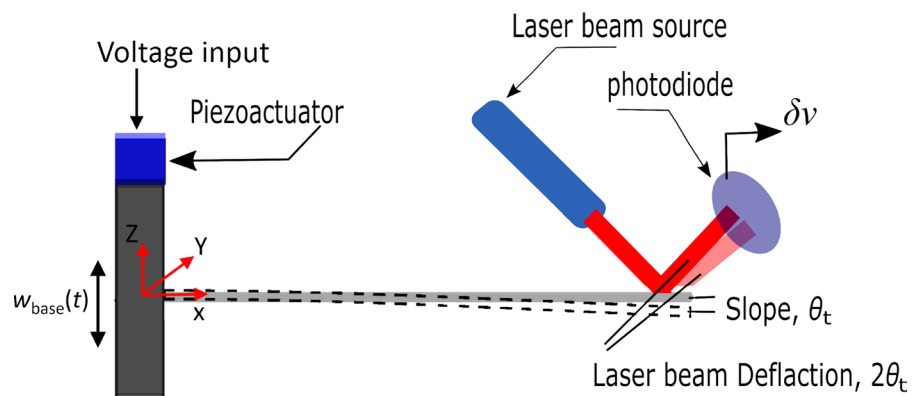
Material	Silicon
Density	2350 kg/m ³
Young's modulus	169 GPa
Length	240 μm
Width	30 μm
Thickness	2 μm

method, an incident laser beam gets reflected from the top surface of the microcantilever beam. The reflection is received using a photodiode or PSD (photo-sensitive detector). Output of the PSD is a function of displacement of the microcantilever beam, which is denoted by δv . It is shown in Fig. 1.

2.1 Closed-loop excitation scheme for parametric actuation

The described model of base excited microcantilever beam has been used for feedback-based parametric excitation. In this method, the sensor output is modulated by a harmonic time function (at frequency 2Ω , where Ω is the frequency of modulation). Further, it is sent as an input to the piezoactuator, which provides transverse displacement to the clamped end. When the frequency of modulation (2Ω) is very near to twice one of the natural frequencies of the cantilever beam, parametric instability occurs. Here, the applied transverse displacement to the clamped end is in the range of nanometers to few micrometers, for which the actuation can be assumed to have linear characteristics. One can see Appendix A for the details about the considered

Fig. 1 Base excited microcantilever model



approach for actuation. A block diagram for feedback-based excitation is shown in Fig. 2.

At micro/nanoscale, the disturbances from the surroundings and the disturbances within actuation and sensing can influence the response of the resonator, or it can also affect the measurement. In the considered MEMS system, thermal forces caused Brownian motion and sensor noise are the significant sources to be considered. Thermal forces acting on the microcantilever in the heat bath have the white power spectral density. Sensor noise depends on different parameters, like the light source, power of laser beam, photodiode circuit, etc. As a result of all the parameters, the sensor noise is found with a flat power spectral density [30–32]. So, thermal forces and sensor noise both are white. Influence of the noises has been analyzed numerically, and the results have been presented in Appendix B. In the block diagram, the dashed red color line indicates the presence of thermal displacement noise in the displacement. The dashed-dotted red line indicates the presence of sensor noise within the sensor output (δv).

Within the closed-loop system, between detection and excitation, some time delay will always be present. There is no differentiation or integration of sensor output required in the considered working model before feeding it back to the piezoactuator. So, the feedback is very quick, and the time delay is very small [21, 22].

With respect to parametric excitation, displacement applied to the clamped end, $w_{\text{base}}(t)$ can be given in the following form.

$$w_{\text{base}}(t) = G_a \delta v \cos(2\Omega t) \quad (1)$$

Characteristics of sensor which measures the response of microstructure play a crucial role in the closed-loop excitation technique.

2.2 Sensor nonlinearity

The sensor output, δv has nonlinear characteristics [29]. Experimental observations show that it can be assumed as a cubic polynomial function of the tip displacement [21]. Coefficients of the nonlinear terms depend on the laser beam diameter and on the relative arrangement of the microcantilever, laser beam source, and photodiode. The sensor output can be represented using the following relationship.

$$\begin{aligned} \delta v &= f(\Delta z), \\ &= c_0 + \sum c_i (\Delta z)^i \end{aligned} \quad (2)$$

Experimental analysis shows that the quadratic term ($c_2(\Delta z)^2$) does not have any effect on the resonant response [21], and the constant term (c_0) also will not affect the excitation. Taking $2G$ as the overall gain, the expression for base excitation is simplified.

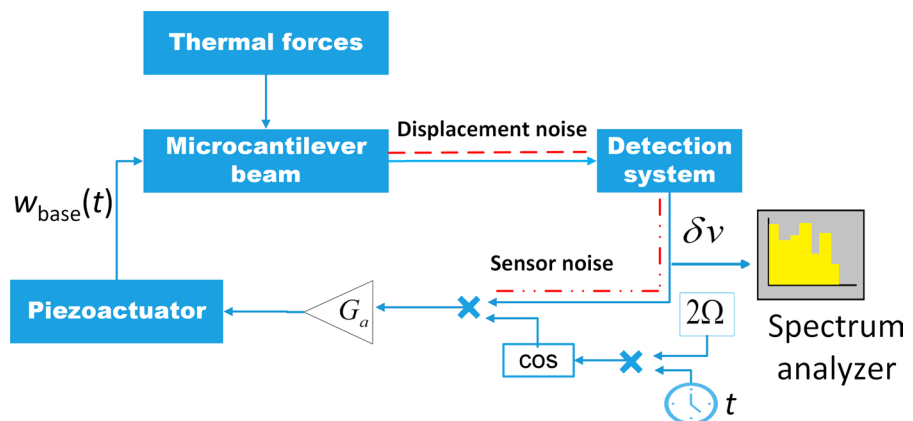
$$\begin{aligned} w_0(t) &= 2G(w(L, t) + \alpha_c w(L, t)^3) \cos(2\Omega t) \\ &\quad + 2G_d \cos(\Omega t) \end{aligned} \quad (3)$$

Equivalent sensor nonlinearity for the cubic term is given by α_c which has a negative value. Here, sensor nonlinearity can also be eliminated for a certain range of displacement of the microcantilever beam. It has been experimentally demonstrated before [33]. Extracting large data for δv and Δz values, a relationship can be established between photodiode output and cantilever displacement, such that

$$\Delta z = f^{-1}(\delta v). \quad (4)$$

However, the mass sensing scheme proposed in this article can work for larger sensor nonlinearity also.

Fig. 2 Block diagram of the closed-loop system



3 Mathematical modelling and analysis

As discussed in Sect. 1, nonlinear behavior in MEMS resonator is inevitable many times. In the present work, our goal is to analyze the dynamics of microcantilever beam parametrically excited for large deflection.

Governing equation of microcantilever beam under large deflection is given below, where the geometric and inertial nonlinearities are considered. Effect of microsize on the dynamics of a cantilever beam model is also taken into consideration.

$$\begin{aligned} \rho A \frac{\partial^2 w}{\partial t^2} + C_d \frac{\partial w}{\partial t} + (EI + l_s^2 \mu A) w'''' + \left(EI + \frac{l_s^2 \mu A}{4} \right) (w' w''^2 + w'^2 w''')' - l_s^2 \mu I \left(\frac{3}{4} w' w''^2 + w' w'' w'''' + \frac{1}{4} w'^2 w''''' \right)' + \frac{\rho A}{2} \left(w' \int_L^x \frac{\partial^2}{\partial t^2} \int_0^x w'^2 dx dx \right)' = 0 \end{aligned} \quad (5)$$

Here the symbols ρ, A, E, I, L have usual significance, and C_d, μ are the damping coefficient and modulus of rigidity respectively. In the above equation, the fourth and fifth terms represent geometric nonlinearity due to large deflection, and the sixth term represents inertial nonlinearity. Microscale effects on the dynamics of microbeam are represented by the length scale parameter, l_s , and it is not constant but varies with size [34]. Using modified couple stress theory, size effect has been taken into consideration for Euler–Bernoulli beam [35], Timoshenko beam [36], multiple-layered microbeam [37], etc. For more details about the governing equation, readers are referred to see [38, 39]. Boundary condition for the applied base excitation has been given before Eq. (3), and other boundary conditions are given below.

$$\begin{aligned} \frac{\partial w}{\partial x} = 0 \text{ at } x = 0, \text{ and } \frac{\partial^2 w}{\partial x^2} = 0, \\ \frac{\partial^3 w}{\partial x^3} = 0 \text{ at } x = L \end{aligned} \quad (6)$$

Nondimensionalization of Eq. (5) is carried out taking, $x = \hat{x}L$, $w = \hat{w}L$ and $t = \hat{t}/\bar{\omega}_n$.

$$\begin{aligned} \frac{\partial^2 \hat{w}}{\partial \hat{t}^2} (1 + \delta m \delta(\hat{x} - 1)) + \nu \frac{\partial \hat{w}}{\partial \hat{t}} + C_0 (1 + \eta) \hat{w}'''' + \alpha_g C_0 \left(1 + \frac{\eta}{4} \right) [\hat{w}' \hat{w}''^2 + \hat{w}'^2 \hat{w}''']' - \alpha_g C_0 \frac{\eta \xi}{4} [3 \hat{w}' \hat{w}''^2 + 4 \hat{w}' \hat{w}'' \hat{w}'''' + \hat{w}'^2 \hat{w}''''']' + \alpha_i \left[\hat{w}' \int_1^{\hat{x}} (1 + \delta m \delta(\hat{x} - 1)) \int_0^{\hat{x}} \left(\frac{\partial \hat{w}'}{\partial \hat{t}} + \hat{w}' \frac{\partial^2 \hat{w}'}{\partial \hat{t}^2} \right) d\hat{x} d\hat{x} \right]' = 0 \end{aligned} \quad (7)$$

Here $\eta = \frac{\mu A l_s^2}{EI}$, $\xi = \frac{I}{AL^2}$, $\nu = \frac{C_d}{\rho A \bar{\omega}_n}$, and $C_0 = \frac{EI}{\rho A \bar{\omega}_n^2 L^4}$. External mass, Δm added on the tip is also considered in the above equation, which is given by $\delta m = \frac{\Delta m}{\rho AL}$. Nonlinearity coefficients for geometric and inertial nonlinearities are represented as α_g and α_i respectively. Nondimensionalized form of the boundary conditions is given here.

$$\begin{aligned} \hat{w}(0, \hat{t}) = 2G(\hat{w}(1, \hat{t}) + \alpha \hat{w}(1, \hat{t})^3) \cos(2\hat{\Omega}\hat{t}) + 2\hat{G}_d \cos(\hat{\Omega}\hat{t}), \end{aligned} \quad (8a)$$

$$\frac{\partial \hat{w}}{\partial \hat{x}}(0, \hat{t}) = 0 \text{ and,} \quad (8b)$$

$$\frac{\partial^2 \hat{w}}{\partial \hat{x}^2}(1, \hat{t}) = \frac{\partial^3 \hat{w}}{\partial \hat{x}^3}(1, \hat{t}) = 0, \quad (8c)$$

where $\hat{\Omega} = \Omega/\bar{\omega}_n$, $\alpha = \alpha_c L^2$ and $\hat{G}_d = G_d/L$. α is the parameter for sensor or feedback nonlinearity for the nondimensionalized case.

3.1 Perturbation approach

Method of multiple scales has been applied to study the resonant behaviour of the microcantilever beam. For convenience, all the overhead signs will be dropped in the further procedure. $w(x, t)$ is assumed as $w(x, t; \epsilon) = w_0(x, T_0, T_1) + \epsilon w_1(x, T_0, T_1)$.

Substituting the expression Eq. (9) into Eq. (7), equations with ϵ^0 and ϵ^1 order terms are written below. Here, the higher-order terms are neglected.

$$\epsilon^0 : D_0^2 w_0 + C_0 (1 + \eta) \frac{\partial^4 w_0}{\partial x^4} = 0 \quad (10)$$

$$\begin{aligned}
e^1 : D_0^2 w_1 + C_0(1 + \eta)w_1'''' = \\
- \delta m_1 D_0^2 w_0 \delta(x-1) - v_1 D_0 w_0 - 2D_0 D_1 w_0 \\
- \alpha_{g1} C_0 \left(1 + \frac{\eta}{4}\right) [w_0' w_0''^2 + w_0'^2 w_0''']' \\
+ \alpha_{g1} C_0 \frac{\eta \xi}{4} [3w_0' w_0''^2 + 4w_0' w_0'' w_0'''' + w_0'^2 w_0''''']' \\
- \alpha_{i1} \left[w_0' \int_1^x \int_0^x ((D_0 w_0')^2 + w_0' D_0^2 w_0') dx dx \right]' \quad (11)
\end{aligned}$$

Here damping coefficient, excitation gains and the added mass have been considered taking, $v = \epsilon v_1$, $G = \epsilon G_1$, $G_d = \epsilon G_{d1}$ and $\delta m = \epsilon \delta m_1$, respectively. The nonlinearity coefficients are written as, $\alpha_g = \epsilon \alpha_{g1}$, $\alpha_i = \epsilon \alpha_{i1}$. Further, substituting Eq. (9) into the boundary conditions Eq. (8), following conditions can be derived for $w_0(x, T_0, T_1)$.

$$\begin{aligned}
w_0(0, T_0, T_1) = w_0'(0, T_0, T_1) \\
= w_0''(1, T_0, T_1) = w_0'''(1, T_0, T_1) = 0 \quad (12)
\end{aligned}$$

Similarly, the boundary conditions can be stated for $w_1(x, T_0, T_1)$.

$$\begin{aligned}
w_1(0, T_0, T_1) = 2G_1 \cos(2\Omega T_0) \\
(w_0(1, T_0, T_1) + \alpha w_0(1, T_0, T_1)^3) + 2G_{d1} \cos(\Omega T_0) \quad (13a)
\end{aligned}$$

$$w_1'(0, T_0, T_1) = w_1''(1, T_0, T_1) = w_1'''(1, T_0, T_1) = 0 \quad (13b)$$

Here parametric and direct excitation both are applied to drive the microcantilever beam into one particular mode. So, the expression for $w_0(x, T_0, T_1)$ can be assumed as

$$w_0(x, T_0, T_1) = (A_n e^{i\omega_n T_0} + \bar{A}_n e^{-i\omega_n T_0}) Y_n(x). \quad (14)$$

Here ω_n is the n th natural frequency of the nondimensionalized cantilever beam, and $Y_n(x)$ is the modal function for the respective mode. In the case of parametric excitation, the amplitude for a specific mode is amplified, and the amplitudes for other natural frequencies are suppressed. So, in the above expression, only the n th mode is considered.

Substituting Eq. (14) into Eq. (10), one can get the eigenvalue problem for microcantilever beam.

$$C_0(1 + \eta)Y_n''''(x) - \omega_n^2 Y_n(x) = 0, \quad (15)$$

Here $Y_n(x)$ can be given as

$$\begin{aligned}
Y_n(x) = c_1 \\
\left(\cos(\zeta_n x) - \cosh(\zeta_n x) - \frac{\cos(\zeta_n) + \cosh(\zeta_n)}{\sin(\zeta_n) + \sinh(\zeta_n)} (\sin(\zeta_n x) \right. \\
\left. - \sinh(\zeta_n x)) \right), \quad (16)
\end{aligned}$$

where $\zeta_n^4 = \frac{\omega_n^2}{C_0(1+\eta)}$. Here, $Y_n(x)$ is normalized such that, $\int_0^1 Y_n(x) Y_n(x) dx = 1$. Now, again substituting the expressions Eq. (14) into Eq. (11), one can get,

$$\begin{aligned}
D_0^2 w_1 + C_0(1 + \eta)w_1'''' = e^{i\omega_n T_0} (\omega_n^2 \delta m_1 \delta(x-1) A_n \\
- 2i\omega_n D_1 A_n - i v_1 \omega_n A_n) Y_n(x) \\
+ 2\alpha_{i1} \omega_n^2 \left[Y_n' \int_1^x \int_0^x Y_n'^2 dx dx \right]' (A_n^3 e^{3i\omega_n T_0} \\
+ A_n^2 \bar{A}_n e^{i\omega_n T_0}) \\
+ \alpha_{g1} C_0 \left[- \left(1 + \frac{\eta}{4}\right) (Y_n' Y_n''^2 + Y_n'^2 Y_n''')' \right. \\
\left. + \frac{\eta \xi}{4} (3Y_n' Y_n''^2 + 4Y_n' Y_n'' Y_n'''' + Y_n'^2 Y_n''''')' \right] \times \\
(A_n^3 e^{3i\omega_n T_0} + 3A_n^2 \bar{A}_n e^{i\omega_n T_0}) + cc \quad (17)
\end{aligned}$$

One can assume the solution for $w_1(x, T_0, T_1)$.

$$w_1(x, T_0, T_1) = \phi(x, T_1) e^{i\omega_1 T_0} + \bar{\phi}(x, T_1) e^{-i\omega_1 T_0}, \quad (18)$$

Substituting it into Eq. (17), and equating the coefficients of $e^{i\omega_1 T_0}$, following equation can be derived.

$$\begin{aligned}
- \omega_n^2 \phi(x, T_1) + C_0(1 + \eta)\phi''''(x, T_1) \\
= (\omega_n^2 \delta m_1 \delta(x-1) A_n - 2i\omega_n D_1 A_n - i v_1 \omega_n A_n) Y_n(x) \\
+ 2\alpha_{i1} \omega_n^2 A_n^2 \bar{A}_n \left[Y_n' \int_1^x \int_0^x Y_n'^2 dx dx \right]' + 3\alpha_{g1} C_0 A_n^2 \bar{A}_n \\
\times \left[- \left(1 + \frac{\eta}{4}\right) (Y_n' Y_n''^2 + Y_n'^2 Y_n''')' \right. \\
\left. + \frac{\eta \xi}{4} (3Y_n' Y_n''^2 + 4Y_n' Y_n'' Y_n'''' + Y_n'^2 Y_n''''')' \right] \quad (19)
\end{aligned}$$

Multiplying Eq. (19) by $Y_n(x)$ and integrating from 0 to 1, one can get the following equation.

$$\begin{aligned}
\int_0^1 Y_n(x) (-\omega_n^2 \phi(x, T_1) + C_0 \phi''''(x, T_1)) dx \\
= \omega_n^2 \delta m_1 A_n Y_n(1)^2 - 2i\omega_n \left(D_1 A_n + \frac{v_1}{2} A_n \right) \\
+ A_n^2 \bar{A}_n F_N, \quad (20)
\end{aligned}$$

where $F_N(x)$ contains all the nonlinear terms which are present in the governing equation. It can be given as

$$\begin{aligned} F_N = & 3\alpha_{g1}C_0 \int_0^1 Y_n(x) \left[-\left(1 + \frac{\eta}{4}\right)(Y_n'Y_n''^2 + Y_n'^2Y_n''')' \right] dx \\ & + 3\alpha_{g1}C_0 \int_0^1 Y_n(x) \left[\frac{\eta\xi}{4}(3Y_n'Y_n''^2 + 4Y_n'Y_n''Y_n'''' + Y_n'^2Y_n''''')' \right] dx \\ & + 2\alpha_{i1}\omega_n^2 \int_0^1 Y_n(x) \left[Y_n' \int_1^x \int_0^x Y_n'^2 dx dx \right]' dx. \end{aligned} \quad (21)$$

Using the boundary conditions for w_0 and w_1 , left hand side of Eq. (20) can be simplified. one can get following relationship through integral by parts.

$$\begin{aligned} \int_0^1 \phi''''(x, T_1) Y_n(x) dx &= \phi(0, T_1) Y_n'''(0) \\ &+ \int_0^1 \phi(x, T_1) Y_n''''(x) dx \end{aligned} \quad (22)$$

Equation (20) can be simplified using the above relation and the eigenvalue problem, stated as Eq. (15).

$$\begin{aligned} C_0(1 + \eta)\phi(0, T_1)Y_n'''(1) &= \omega_n^2\delta m_1 A_n Y_n(1)^2 \\ &- 2i\omega_n \left(D_1 A_n + \frac{\nu_1}{2} A_n \right) + A_n^2 \bar{A}_n F_N \end{aligned} \quad (23)$$

$\phi(0, T_1)$ contains the necessary terms for the given base excitation. It can be calculated from the applied displacement boundary conditions. Substituting the expressions for w_0 and w_1 into Eq. (13), and equating the coefficients of $e^{i\omega_n T_0}$, after some algebraic manipulations, following relationship can be derived.

$$\begin{aligned} \phi(0, T_1) = & G_1 Y_n(1) \left(e^{2i\sigma T_1} (\bar{A}_n + 3\alpha_n \bar{A}_n^2 A_n) \right. \\ & \left. + e^{-2i\sigma T_1} \alpha_n A_n^3 \right) + G_{d1} e^{i\sigma T_1} \end{aligned} \quad (24)$$

Here $\alpha_n = Y_n(1)^2 \alpha$ and $\Omega = \omega_n + \epsilon\sigma$. The derived expression for $\phi(0, T_1)$ can be substituted into Eq. (23) and following solvability condition can be derived.

$$\begin{aligned} g \left(e^{2i\sigma T_1} (\bar{A}_n + 3\alpha_n \bar{A}_n^2 A_n) + e^{-2i\sigma T_1} \alpha_n A_n^3 \right) &+ g_d e^{i\sigma T_1} \\ &= \omega_n \delta m_1 A_n \frac{Y_n(1)^2}{2} - i \left(D_1 A_n + \frac{\nu_1}{2} A_n \right) + \frac{A_n^2 \bar{A}_n}{2\omega_n} F_N \end{aligned} \quad (25)$$

where $g = \frac{1}{2\omega_n} G_1 Y_n(1) Y_n''''(0) C_0 (1 + \eta)$ and $g_d = \frac{1}{2\omega_n} G_{d1} Y_n''''(0) C_0 (1 + \eta)$. To study the amplitude

frequency characteristics, one can assume $A_n(T_1) = \frac{1}{2} a_n(T_1) e^{i\beta(T_1)}$. That is substituted into Eq. (25), and after some algebraic manipulations, one can

easily get the simplified form of the solvability condition.

$$\begin{aligned} g \left(e^{2i(\sigma T_1 - \beta(T_1))} \left(a_n + \frac{3\alpha_n a_n^3}{4} \right) + e^{-2i(\sigma T_1 - \beta(T_1))} \frac{\alpha_n a_n^3}{4} \right) \\ + 2g_d e^{i(\sigma T_1 - \beta(T_1))} = \omega_n \delta m_1 a_n \frac{Y_n(1)^2}{2} \\ - i \left(D_1 a_n + i a_n D_1 \beta(T_1) + \frac{\mu_1}{2} a_n \right) \\ + \frac{a_n^3}{8\omega_n} F_N \end{aligned} \quad (26)$$

As a general practice, Taking, $\beta(T_1) = \sigma T_1 - \gamma(T_1)$, the above equation can be brought into the following first-order coupled equations.

$$\begin{aligned} a_n D_1 \gamma &= (\sigma + \omega_n \delta m_1 \frac{Y_n(1)^2}{2}) a_n + \frac{a_n^3}{8\omega_n} F_N \\ &- g \cos(2\gamma) (a_n + \alpha_n a_n^3) - 2g_d \cos(\gamma) \end{aligned} \quad (27a)$$

$$\begin{aligned} D_1 a_n &= -\frac{\nu_1}{2} a_n \\ &- g \sin(2\gamma) (a_n + \frac{\alpha_n}{2} a_n^3) - 2g_d \sin(\gamma) \end{aligned} \quad (27b)$$

For steady state conditions ($D_1 a_n = D_1 \gamma = 0$), the relationship between a_n and excitation parameters, like G_1, Ω, α_n and damping parameter ν_1 can be derived as follows.

$$\begin{aligned} \left(\frac{\nu_1}{2 + \alpha_n a_n^2} \right)^2 a_n^2 + \left(\frac{\sigma + \omega_n \delta m_1 \frac{Y_n(1)^2}{2} + \frac{a_n^2}{8\omega_n} F_N}{1 + \alpha_n a_n^2} \right)^2 \\ a_n^2 = g^2 a_n^2 \end{aligned} \quad (28)$$

Here only parametric excitation is considered ($g_d = 0$). In the case of solely resonant or direct excitation, the amplitude-frequency relationship can also be stated.

$$\frac{v_1^2 a_n^2}{4} + \left(\sigma + \omega_n \delta m_1 \frac{Y_n(1)^2}{2} + \frac{a_n^2}{8\omega_n} F_N \right)^2 a_n^2 = 4g_d^2 \quad (29)$$

One can get the frequency-amplitude behaviour using the Eq. (28) and Eq. (29). System of first order coupled Eq. (27) can be converted into Cartesian format $(x_n(T_1), y_n(T_1))$ for $x_n = a_n \cos \gamma$ and $y_n = a_n \sin \gamma$. Here, only parametric excitation is evaluated ($g_d = 0$). Also the mass deposition isn't considered ($\delta m = 0$).

$$D_1 x_n = -\frac{v_1}{2} x_n - \sigma y_n - \frac{x_n^2 + y_n^2}{8\omega_n} y_n F_N - g(y_n + \alpha_n y_n^3) \quad (30a)$$

$$D_1 y_n = -\frac{v_1}{2} y_n + \sigma x_n + \frac{x_n^2 + y_n^2}{8\omega_n} x_n F_N - g(x_n + \alpha_n x_n^3) \quad (30b)$$

From the expression Eq. (28), one can get all the fixed-points, and their stability can be determined using the first order equations in the Cartesian form Eq. (30). To accomplish this, we let

$$x_n = x_{n0} + x_{n1} \\ y_1 = y_{n0} + y_{n1},$$

where $x_{n0} = a_{n0} \cos \gamma_0$ and $y_{10} = a_{n0} \sin \gamma_0$. Here, a_{n0} refers to the a_n value for the fixed-point. It can be calculated using the relationship Eq. (28) for the given values of G, v, σ and α . For small values of x_{n1} and y_{n1} , first order coupled equations in the Cartesian form Eq. (30) can be written in the matrix form.

$$\begin{Bmatrix} D_1 x_{n1} \\ D_1 y_{n1} \end{Bmatrix} = \mathbf{J} \begin{Bmatrix} x_{n1} \\ y_{n1} \end{Bmatrix}, \quad (31)$$

and the coefficient matrix can be given as

$$\mathbf{J} = \begin{bmatrix} -\frac{v_1}{2} - a_0^2 \sin(2\gamma_0) \frac{F_N}{8\omega_n} & -\sigma - g - a_{n0}^2 \frac{F_N}{8\omega_n} - 2y_{n0}^2 \left(\frac{F_N}{8\omega_n} + 1.5g\alpha_n \right) \\ \sigma - g + a_{n0}^2 \frac{F_N}{8\omega_n} + 2x_{n0}^2 \left(\frac{F_N}{8\omega_n} - 1.5g\alpha_n \right) & -\frac{v_1}{2} + a_0^2 \sin(2\gamma_0) \frac{F_N}{8\omega_n} \end{bmatrix}. \quad (32)$$

To determine the stability of all the fixed points, \mathbf{J} can be further simplified. Using the system of equations

in the polar form Eq. (27), for the steady-state condition, one can calculate $\sin(2\gamma_0)$ and $\cos(2\gamma_0)$. Here, if the determinant of \mathbf{J} is positive (negative), then the fixed point is considered stable (unstable). The stability characteristics are described in Sect. 5.

4 Numerical analysis

In this section, the nondimensional integro-partial differential Eq. (7) has been analyzed numerically. Here, two schemes have been used for numerical analysis: (i) generalized differential quadrature method (GDQM), and (ii) Galerkin method. For numerical analysis of cantilever beam with large deflection, the nondimensionalized form of governing equation Eq. (7) is considered in the relative frame of reference. For displacement of the cantilever beam relative to the clamped end, the governing equation can be modified to the following.

$$\begin{aligned} (1 + \delta m \delta(x-1)) \frac{\partial^2 \bar{w}}{\partial t^2} + v \frac{\partial \bar{w}}{\partial t} + C_0(1 + \eta) \bar{w}'''' \\ + \alpha_g C_0 \left(1 + \frac{\eta}{4} \right) [\bar{w}' \bar{w}''^2 + \bar{w}^2 \bar{w}''']' \\ + \alpha_i \left[\bar{w}' \int_1^x (1 + \delta m \delta(x-1)) \right. \\ \left. \int_0^x \left(\frac{\partial \bar{w}'}{\partial t} + \bar{w}' \frac{\partial^2 \bar{w}'}{\partial t^2} \right) dx \right]' \\ - \alpha_g C_0 \frac{\eta^{\frac{\xi}{2}}}{4} [3\bar{w}' \bar{w}''^2 + 4\bar{w}' \bar{w}'' \bar{w}'''' + \bar{w}^2 \bar{w}''''']' \\ = -(1 + \delta m \delta(x-1)) \frac{\partial^2 w_{\text{base}}}{\partial t^2} - v \frac{\partial w_{\text{base}}}{\partial t} \end{aligned} \quad (33)$$

$\bar{w}(x, t)$ is the relative displacement of the microcantilever beam with respect to the base, and $w_{\text{base}}(t)$ is the transverse displacement given to the base. The total displacement of cantilever beam $w(x, t)$ is given as

$$w(x, t) = w_{\text{base}}(t) + \bar{w}(x, t), \quad (34)$$

Applied base excitation, w_{base} is calculated from the displacement of the cantilever beam,

$$w_{\text{base}}(t + dt) = 2G \cos(2\Omega t) (w(1, t) + \alpha w(1, t)^3), \quad (35)$$

where free end displacement $w(1, t)$ is calculated as

$$w(1, t) = \bar{w}(1, t) + w_{\text{base}}(t). \quad (36)$$

Here dt is the step size for numerical simulation. Simulation for both the numerical methods is carried out using the well-known constant acceleration Newmark-beta scheme [40].

4.1 GDQM

Differential quadrature method is a very useful technique for numerical analysis of partial differential equation (PDE) [41]. It can handle nonlinear PDEs also very efficiently. In DQM, a certain number of discrete points are chosen within the domain. Partial derivative at the given discrete point can be approximated as a weighted sum of the function evaluated at all the discrete points. GDQM is a well-known approach found in the literature. It has been utilized for static and dynamic analysis of beam [42], plate [43], beam with nonlinear boundary conditions [44], etc. With GDQM, r th order partial derivative is approximated as,

$$\frac{\partial^r w(x, t)}{\partial x^r} \Big|_{x=\eta_i} = \sum E_{ij}^{(r)} W_j(t), \quad \text{where, } j = 1, 2, \dots, N_{DQ}. \quad (37)$$

Here $E_{ij}^{(r)}$ is the weighting coefficient matrix, and N_{DQ} is the total number of discrete points considered within the domain. η_i is a grid point. For nondimensionalized model of cantilever beam, grid points are chosen using Chebyshev-Gauss-Lobatto distribution. That is given as,

$$\eta_i = 0.5 \left(1 - \cos \left(\pi \frac{(i-1)}{N_{DQ}-1} \right) \right), \quad \text{where } i = 1, 2, \dots, N_{DQ}. \quad (38)$$

For applying GDQM, the weighting coefficients can be calculated very easily using the Lagrange polynomial [44]. Expression for the first order derivative, $E_{ij}^{(1)}$ is given here.

$$E_{ij}^{(1)} = \frac{\prod_{m=1, m \neq i}^{N_{DQ}} (x_i - x_m)}{(x_i - x_j) \prod_{m=1, m \neq j}^{N_{DQ}} (x_j - x_m)}, \quad (39a)$$

for $i, j = 1, \dots, N_{DQ}$, and, $i \neq j$

$$E_{ii}^{(1)} = - \sum_{m=1}^{m=N_{DQ}} E_{im}^{(1)}, \quad \text{for } i = 1, \dots, N_{DQ} \quad (39b)$$

The weighting coefficients matrices for higher order derivatives can be determined by matrix multiplication [45, 46].

$$E^{(r)} = E^{(1)} E^{(r-1)}, \quad (r > 1) \quad (40)$$

Weighting coefficient matrices for higher order derivatives can be calculated using the formulae Eqs. (39) and (40). Here the boundary conditions will be considered while calculating weighting coefficient matrices. The boundary conditions that need to be satisfied are

$$\bar{w}(0, t) = \bar{w}'(0, t) = \bar{w}''(1, t) = \bar{w}'''(1, t) = 0. \quad (41)$$

There are various techniques for considering boundary conditions in the differential quadrature based numerical analysis [45]. The procedure followed in the present study is through modification of the weighting coefficient matrices [46]. Here, zero displacement and zero slope condition at the clamped end can be satisfied just by neglecting the first column and first row respectively. The remaining boundary conditions, which are defined at the free end will be used for calculating weighting coefficient matrices.

$$E_{ij}^{(2)} = \sum_{k=2}^{k=N_{DQ}} E_{ik}^{(1)} E_{kj}^{(1)}, \quad (42)$$

$$\text{where } \sum_{j=2}^{j=N_{DQ}} E_{N_{DQ}j}^{(2)} W_j = 0$$

$$E_{ij}^{(3)} = \sum_{k=2}^{k=N_{DQ}} E_{ik}^{(1)} E_{kj}^{(2)}, \quad (43)$$

$$\text{where } \sum_{j=2}^{j=N_{DQ}} E_{N_{DQ}j}^{(3)} W_j = 0$$

Here W_j is the relative displacement at η_j grid point with respect to the clamped end or grid point, η_1 . Here, microscale effect and addition of mass (δm) is not considered while carrying out the simulation. The nonlinear integro-partial differential equation Eq. (33) can be discretized into the following system of equations.

$$\begin{aligned}
& \ddot{W}_i + \nu \dot{W}_i + C_0 \sum_{j=2}^{N_{DQ}} E_{ij}^{(4)} W_j + \alpha_g C_0 \\
& \times \left[\left(\sum_{j=2}^{N_{DQ}} E_{ij}^{(2)} W_j \right)^3 + 4 \sum_{j,k,l=2}^{N_{DQ}} E_{ij}^{(1)} E_{ik}^{(2)} E_{il}^{(3)} W_j W_k W_l \right. \\
& \left. + \left(\sum_{j=2}^{N_{DQ}} E_{ij}^{(2)} W_j \right)^2 \sum_{j=2}^{N_{DQ}} E_{ij}^{(4)} W_j \right] - \alpha_i \sum_{j=2}^{N_{DQ}} E_{ij}^{(1)} \\
& \times \left[\left(\sum_{k=2}^{N_{DQ}} E_{jk}^{(1)} W_k \right) \left(\sum_{k,l=2}^{N_{DQ}} H_{jk} I_{kl} \left(\sum_{p=2}^{N_{DQ}} E_{lp}^{(1)} \dot{W}_p \right)^2 \right. \right. \\
& \left. \left. + \sum_{p,q=2}^{N_{DQ}} E_{lp}^{(1)} E_{lq}^{(1)} W_p \dot{W}_q \right) \right] \\
& = -(\dot{W}_{\text{base}} + \nu \dot{W}_{\text{base}}), \tag{44}
\end{aligned}$$

where $i = 2, 3, \dots, N_{DQ}$. To discretize the integro partial differential terms in Eq. (33), Newton-Cotes formula have been used [47].

$$H_{pq} = \int_{\eta_p}^1 \prod_{m=p, m \neq q}^{N_{DQ}} \frac{x - \eta_m}{(\eta_q - \eta_m)}, \tag{45}$$

$$\begin{aligned}
I_{pq} &= \int_0^{\eta_p} \prod_{m=1, m \neq q}^p \frac{x - \eta_m}{(\eta_q - \eta_m)}, \\
&\text{for } p, q = 1, 2, \dots, N_{DQ}
\end{aligned} \tag{46}$$

For numerical analysis based on GDQM, the system of equations Eq. (44) will be used.

4.2 Galerkin method

To get reduced order model of the governing equation, Galerkin procedure has also been found extremely useful. Through this method both micro-scale effects and addition of mass have been considered within the analysis. Using Eq. (33), $\bar{w}(x, t)$, can be approximated as

$$\bar{w}(x, t) = \sum_{j=1}^M Y_j(x) q_j(t), \tag{47}$$

where $Y_j(x)$ is the j th eigenfunction for a linear Euler–Bernoulli cantilever beam, and $q_j(t)$ is the j th generalized coordinate. Governing equation, Eq. (33) can be discretized using the approximation Eq. (47) as following.

$$\begin{aligned}
& \sum_{j=1}^M \left(\int_0^1 Y_i \mu_m(x) Y_j dx \right) \ddot{q}_j + \nu \sum_{j=1}^M \left(\int_0^1 Y_i Y_j dx \right) \dot{q}_j \\
& + C_0 (1 + \eta) \sum_{j=1}^M \left(\int_0^1 Y_i Y_j'''' dx \right) \\
& q_j + \alpha_i \sum_{j,k,l=1}^M \int_0^1 Y_i \left[Y_j' \int_1^x \mu_m(x) \int_0^x Y_k' Y_l' dx dx \right]' \\
& (q_j \dot{q}_k \dot{q}_l + q_j q_k \dot{q}_l) \\
& + \alpha_g C_0 \left(1 + \frac{\eta}{4} \right) \left\{ \sum_{j,k,l=1}^M \left(\int_0^1 Y_i Y_j'' Y_k'' Y_l'' dx \right) q_i q_j q_l \right. \\
& + \sum_{j,k,l=1}^M \left(\int_0^1 Y_i Y_j' Y_k' Y_l'''' dx \right) \\
& \times q_i q_j q_l + 4 \sum_{j,k,l=1}^M \left(\int_0^1 Y_i Y_j' Y_k'' Y_l'''' dx \right) q_i q_j q_l \\
& - \frac{\eta \xi}{4} \left\{ 3 \sum_{j,k,l=1}^M \int_0^1 Y_i \left(Y_j' Y_k'''' Y_l'''' \right)' dx q_j q_k q_l \right. \\
& + 4 \sum_{j,k,l=1}^M \int_0^1 Y_i \left(Y_j' Y_k'' Y_l'''' \right)' dx q_j q_k q_l \\
& \left. + \sum_{j,k,l=1}^M \int_0^1 Y_i \left(Y_j' Y_k' Y_l'''''' \right)' dx q_j q_k q_l \right\} \\
& = - \int_0^1 Y_i \mu_m(x) dx \dot{W}_{\text{base}} - \int_0^1 Y_i dx \nu \dot{W}_{\text{base}}, \tag{48}
\end{aligned}$$

where $\mu_m(x) = (1 + \delta m \delta(x - 1))$. Above system of equations Eq. (48) will be used for the numerical analysis based on Galerkin scheme.

5 Results and discussion

Outcomes of multiple scales analysis and numerical simulation are discussed here in detail. Effect of different nonlinearities on resonance characteristics is analyzed, and influence of microsize on the dynamics of a microcantilever beam is also presented. Further,

a method of mass detection has been proposed and discussed in detail. In this scheme, the variation in amplitude will give the necessary measure for mass detection. Finally, convergence for the different numerical methods used is shown.

5.1 Stability analysis based on multiple scales

Based on the perturbation approach, stable-unstable behavior of the cantilever beam under parametric excitation is explained here. One can get the fixed points from the formula Eq. (28), and its stability can be analyzed from the first-order differential equations in Cartesian form Eq. (30). Results of stability analysis for parametric excitation in the first and second modes are presented here. Initially, the terms in the governing equation Eq. (7) which describe the microsize effects are neglected for the present stability analysis.

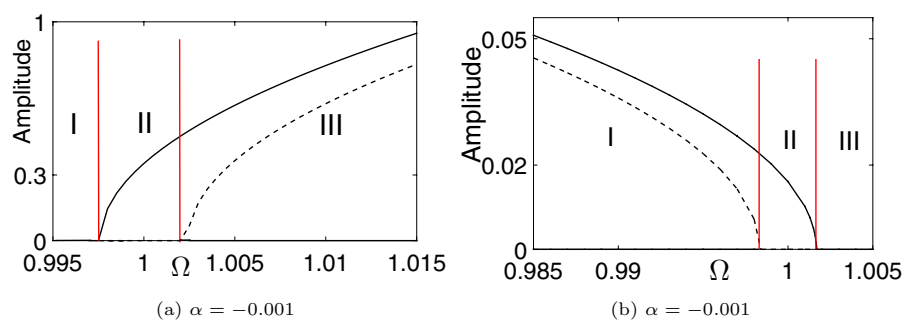
For parametric excitation in the first mode ($\Omega \approx \omega_1$), stable and unstable fixed points are shown in Fig. 3a. Here, we have considered the value of sensor or feedback nonlinearity very small ($\alpha = -0.001$). Discussion for sensor nonlinearity has been presented in Sect. 2.2 for which α is the nondimensionalized parameter. The amplitude-frequency space is divided into three regions. In the first region, only a trivial fixed point exists, which is stable. In the second region, the trivial fixed point becomes unstable. In addition to that, a non-trivial fixed point also exists in the second region, which is stable. The trivial fixed point, which is unstable in the second region, again becomes stable in the third region, whereas the stable non-trivial fixed point remains stable in the third region also. In this region, one more branch of fixed points exists, and these fixed points are unstable. Here, within the third region, the branch of non-trivial

stable fixed points exists even for large Ω values. The resonance characteristics show hardening behavior.

Stability characteristics for parametric excitation in the second mode are shown in Fig. 3b, where the modulation frequency (2Ω) is selected close to twice the second natural frequency ($\Omega \approx \omega_2$). To simplify the analysis, nondimensionalization is carried out in such a way so that the second natural frequency, $\omega_2 = 1$. For parametric excitation in the second mode, the amplitude-frequency curve shows softening behavior due to the increased strength of inertial nonlinearity. The influence of geometric and inertial nonlinearities on resonator dynamics will be discussed further. Here also, the amplitude-frequency space is divided into three regions. In the first region, the trivial fixed point is stable. In addition to that, two non-trivial fixed points exist. One of the two is stable, and another is unstable. In the second region, a non-trivial and a trivial fixed point exists. They are stable and unstable, respectively. Finally, in the third region, only a trivial fixed point exists, which is stable. As realized for parametric excitation in the first mode, here also the same trend follows. The non-trivial fixed point in first region remain stable for $\omega_2 \ll \Omega$.

Here, the branch of stable non-trivial fixed points in the third (first) region for parametric excitation in the first (second) mode exists for Ω values far from the natural frequency. So, according to the carried out perturbation analysis, there will not be any downward jump in amplitude for small values of sensor or feedback nonlinearity. But while carrying out numerical simulation, downward jumps have been reported for parametric excitation in both the modes. That has been discussed further. According to the perturbation analysis, the frequency of downward jump depends on the value of α .

Fig. 3 Stability analysis for parametric excitation (a) in the first mode ($\Omega \approx \omega_1$), and (b) in the second mode ($\Omega \approx \omega_2$)



On increasing the absolute value of α , stability characteristics in the third (first) region for parametric excitation in the first (second) mode change. The branch of stable non-trivial fixed points exists only for a certain range in the described regions. For $\alpha = -4$, the branches of stable and unstable non-trivial fixed points meet each other at point P. That is shown in Fig. 4a. For Ω values between P and P', only trivial stable fixed points exist. At point p', two branches commence. One of them is stable, and another is unstable. Steady-state amplitude value for the stable branch P'P' ' is higher than the maximum possible amplitude value (depends on α). Therefore, it cannot be achieved numerically or experimentally. For $\alpha = -1$ also, two branches commence from a point, but that happens for $\Omega \gg \omega_1$.

Similar trend can be noticed for parametric excitation in the second mode (see Fig. 4b). Branches of stable and unstable fixed points meet each other at points Q and R for $\alpha = -400$ and $\alpha = -200$, respectively. Here, commencing of two new branches happens for $\Omega \ll \omega_2$. From the results of perturbation analysis, it can be stated that with the increase in absolute value of α slope of the amplitude-frequency curve decreases. Also one can notice that the width

of region of parametric instability (region II) remains unchanged.

5.1.1 Comparison with numerical analysis

For the first and second modes, the steady-state amplitude values derived from the perturbation technique are compared with the results of numerical simulation. For numerical study, generalized differential quadrature scheme and Galerkin method are used. The comparison is presented here for $\alpha = -0.001$. Forward and reverse frequency sweeps are carried out during the simulation process. The respective result is shown in Fig. 5a. For the second mode based parametric excitation, the comparison is shown in Fig. 5b. In both cases, an excellent match is found between the steady-state amplitude values derived from multiple scales and the amplitude values calculated using numerical methods for Ω values close to natural frequencies. Among both the methods Galerkin scheme is found with better accuracy. While carrying out numerical simulation using Galerkin method, downward jumps have been reported for parametric excitation in both the modes. But while using GDQM to analyze parametric excitation in the first mode, the simulation fails for a few of the Ω values. That has been marked using black colored stars in Fig. 5a.

While carrying out the numerical analysis for the first mode based parametric excitation, the differential quadrature scheme fails for $\alpha_i = 1$ and $\alpha_g = 1$. Here, numerical analysis is carried out for a larger coefficient of geometric nonlinearity ($\alpha_i = 1$ and $\alpha_g = 2$). The respective results are shown in Fig. 5a. For the other case (parametric excitation in the second mode), $\alpha_i = 1$ and $\alpha_g = 1$ is taken. While carrying out simulation for parametric excitation in the first mode, excitation gain and damping coefficient are chosen as $G = 0.002$ and $\nu = 0.002$. In the case of parametric excitation in the second mode, the respective values are chosen as $G = 0.003$ and $\nu = 0.002$ (see Fig. 5b).

Nonlinear parametric resonance for a large value of α is analyzed using Galerkin scheme. Comparison for parametric excitation in the first mode for $\alpha = -4$ is shown in Fig. 6, where the results of forward and reverse frequency sweep are shown. Steady state amplitude for forward (reverse) frequency sweep is shown using continuous (dashed) red-colored lines. The outcome of numerical analysis for amplitude values within the region of parametric instability is

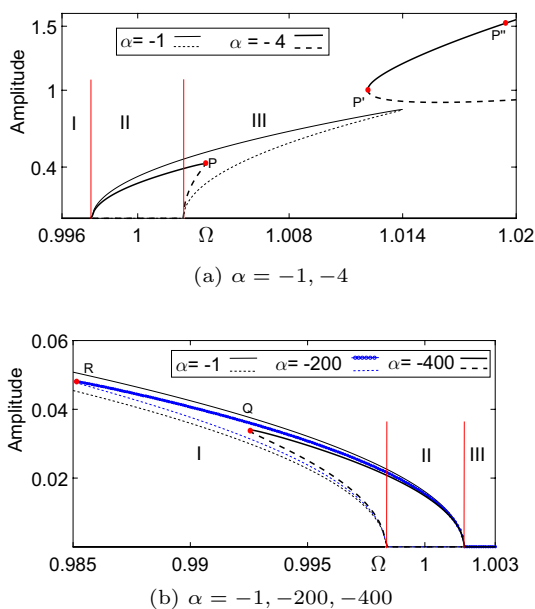
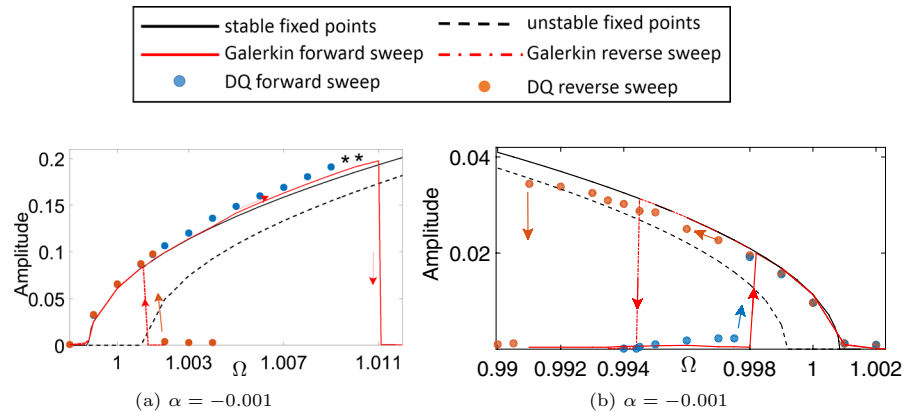


Fig. 4 Stability analysis considering large values of α for parametric excitation (a) in the first mode, and (b) in the second mode

Fig. 5 Comparison of the results of multiple scales and numerical methods for parametric excitation **(a)** in first mode, and **(b)** in the second mode



found with high accuracy, but immediately after the instability region, a downward jump in the amplitude has been noticed. In the case of parametric excitation in the second mode, a very large value of α has been used to demonstrate the effect of sensor nonlinearity.

For $\alpha = -400$, comparison for parametric excitation in the second mode is shown in Fig. 6. Here also, a perfect agreement is found between the outcomes of Galerkin method and multiple scales technique in the region of parametric instability. But while carrying out the reverse sweep, there is an early downward jump in the amplitude. So, a disagreement is noticed in the jump-down frequency for parametric excitation in both the modes. But we are mainly interested in the regime of parametric instability to carry out mass detection, where a very good agreement has been achieved in between numerical simulation and perturbation analysis.

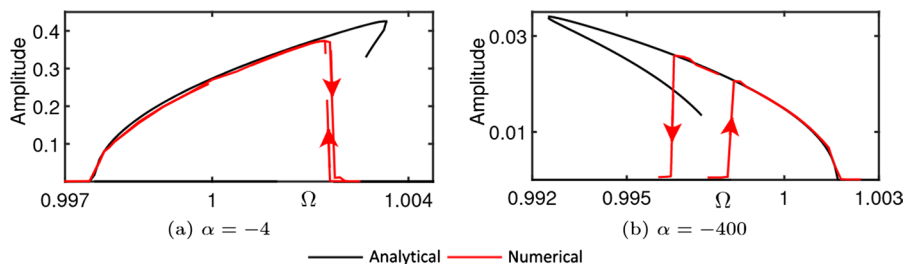
The differential quadrature method fails or gives highly inaccurate results for large values of α . So, it has not been used to analyze the effect of sensor nonlinearity with a large value. The values of parametric excitation gain (G) and damping coefficient (ν) are the same which have been considered for $\alpha = -0.001$.

5.1.2 Influence of geometric and inertial nonlinearities

As discussed in Chapter 2, Large deflection causes axial displacement in the cantilever beam, and coupling of axial and transverse displacement induces geometric nonlinearity [48]. The coupling takes place due to large curvature. Inertial force in the axial direction also generates nonlinear behavior called inertial nonlinearity. For parametric excitation gain, $G = 0.004$ and damping coefficient, $\nu = 0.004$ steady-state amplitude values are calculated using multiple scales analysis and GDQM. They are shown in Fig. 7a, b for geometric and inertial nonlinearities respectively.

Here, the study is carried out for first mode based parametric excitation. For analyzing the effect of geometric nonlinearity, forward frequency sweep is carried out, and for the analysis of inertial nonlinearity, reverse frequency sweep is carried out. Here, only non-trivial stable fixed points values are shown for the comparison. For analyzing the effect of solely geometric nonlinearity ($\alpha_g = 1, \alpha_i = 0$), GDQM fails

Fig. 6 Comparison for larger value of sensor or feedback nonlinearity for parametric excitation **(a)** in the first mode, and **(b)** in the second mode



for certain values of Ω which are far from the natural frequency. Those results are marked by stars.

5.2 Influence of microsize on the dynamics

Effect of microscale on the resonator characteristics has been briefly discussed in Chapter 2. Due to the size effect, natural frequency increases, and the overall nonlinear phenomenon also changes. The microsize effect causes softening nonlinearity. In Fig. 8a, non-trivial stable fixed points are shown for different values of η . Here, $\eta = \frac{\mu A l_s^2}{EI}$ has been used as the parameter for size dependency. Length scale parameter (l_s) strongly depends on thickness or diameter. As the value of η increases, softening behavior due to the size effect becomes strong, and the positive shift in natural frequency also increases. Amplitude-frequency behavior is shown in Fig. 8b. Here, the parameters are taken as $\mu = 65.8$ GPa and $l_s = 0.592$ μm [27, 38]. Results show that the natural frequency shifts on the higher side with the increase in η value, and the nonlinear behavior also shifts from hardening to softening.

5.3 Mass sensing based on the change in amplitude

Most resonator-based mass sensors work on the principle of change in the natural frequency due to mass addition. That needs time-consuming frequency sweep, or a complex phase-locked loop-based oscillator, in which the natural frequency is continuously traced [49]. Here, based on the nonlinear parametric resonance, a novel mass detection scheme is suggested. In this method, the resonator needs to be excited at a constant frequency instead of sweeping the excitation frequency, and continuous tracing of natural frequency is also not required. Here, microscale effect, which causes softening behavior, is not considered, but the proposed scheme of mass detection can be used with hardening as well as softening behavior.

In the range of parametric instability (region II), where a trivial fixed point is unstable, the slope of the amplitude-frequency curve is large. One can see Fig. 9a, b. Here, the amplitude-frequency behavior of parametric (direct) excitation is marked with black (red) colored lines. Continuous (dashed) lines represent branches of stable (unstable) fixed points. One can see that, in a certain region, there is a large variation in the amplitude for parametric

Fig. 7 **a** Hardening effect caused by geometric nonlinearity ($\alpha_g = 1, \alpha_i = 0$), and **b** softening effect caused by inertial nonlinearity ($\alpha_g = 0, \alpha_i = 1$)

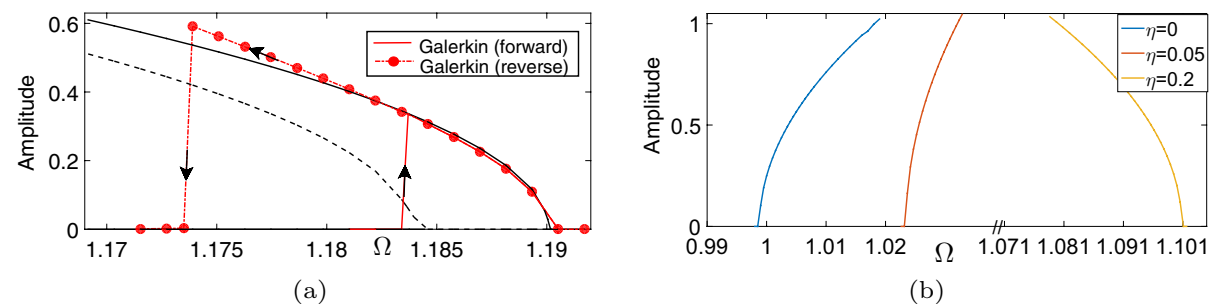
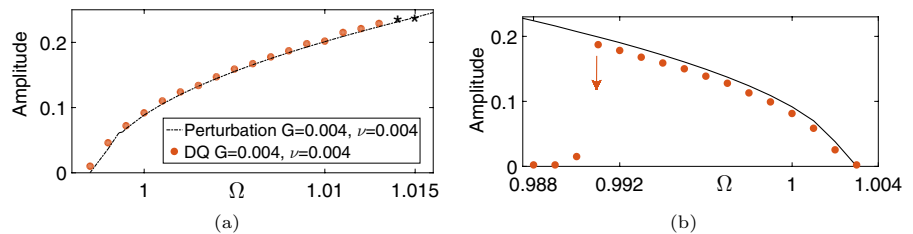


Fig. 8 **a** Steady-state amplitude values for different values of η , and **b** increase in resonance frequency and softening behavior due to microsize effect

excitation in comparison to direct excitation. These regions of parametric instability shown using rectangles of blue coloured dashed lines in Fig. 9a, b are the regions of our interest. If the microcantilever beam can be excited at a certain frequency within this region, then the relative change in the steady-state amplitude due to a negative shift in the natural frequency will be very high. Here, the addition of unknown mass will cause a shift of natural frequency, and so there will be a certain change in the steady-state amplitude. By measuring the variation in the amplitude, added mass can be approximated. Mass sensing based on the variation in the amplitude has been demonstrated before using direct excitation [25], but the parametric instability-based proposed technique can provide superior performance.

The basic principle is to utilize the parametric instability and it is explained with the help of Fig. 9c, d. Amplitude-frequency curves for parametric and direct excitations for the first two modes are compared with each other. The comparison shows that the slope of the curve is very small for direct excitation. Amplitude-frequency curves show hardening (softening) behavior for the excitation in the first (second) mode so that there will be a certain increment (decrement) in the amplitude due to the negative shift of natural frequencies. Shifting of the amplitude for direct and parametric excitation is compared here. Change in the amplitude for parametric excitation (AA') is much larger than for resonant or direct excitation (BB'). Amplitude response for parametric excitation is similar to that of direct excitation in region III (region I) for the first (second) mode.

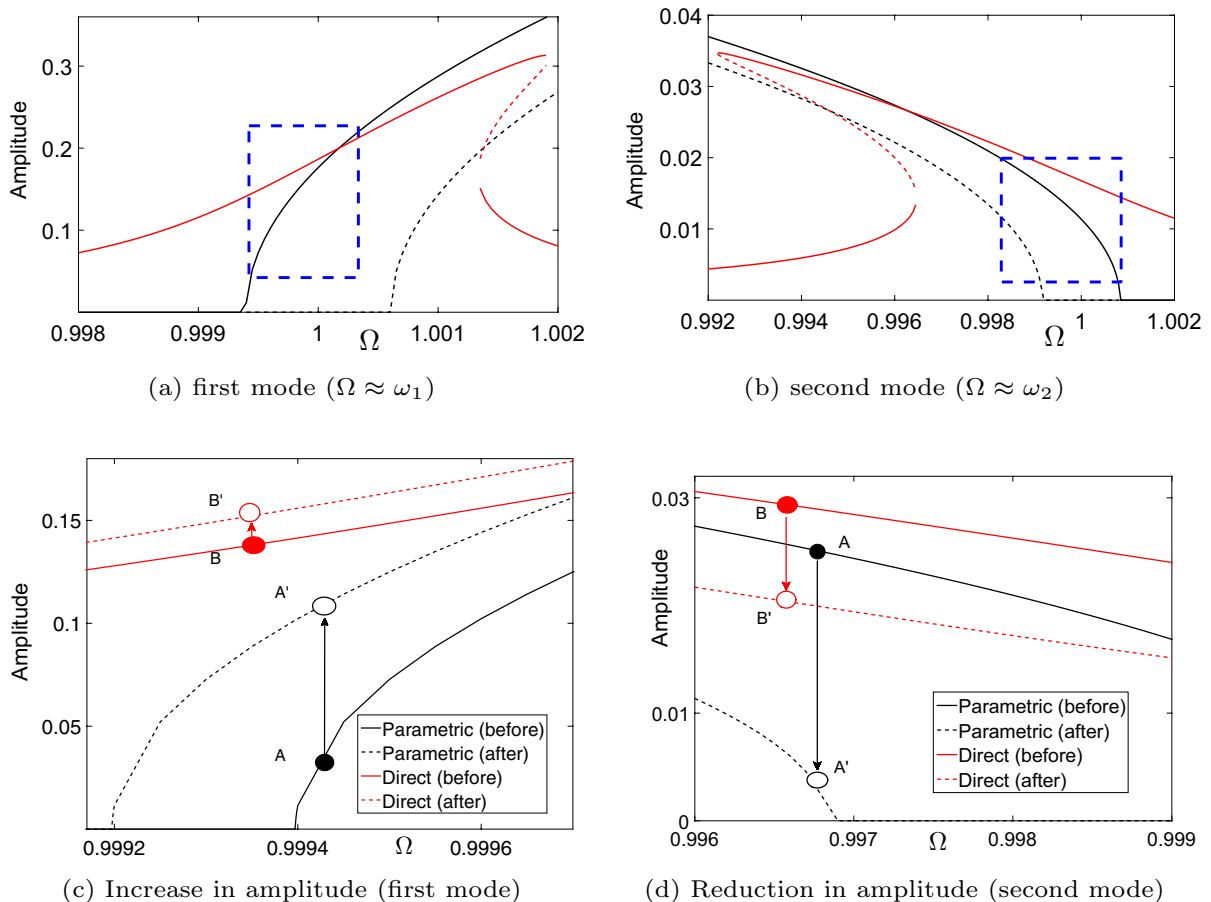


Fig. 9 Comparison of parametric and direct excitation: **a, b** amplitude-frequency response of microcantilever beam, and **c, d** amplitude shift due to mass addition

For some excitation parameters (G, G_d, Ω), relative change in amplitude is mentioned for few values of added mass in Tables 2 and 3. Amplitude values derived from multiple scales technique are compared with results from Galerkin technique. Relative variation in the amplitude is shown with bold text.

5.3.1 Evaluating the sensing technique

The frequency of excitation (or modulation frequency 2Ω) plays a very important role in the proposed technique. To take the advantage of nonlinear parametric resonance, the microcantilver beam should be excited at certain frequency, where the slope of amplitude-frequency curve is high (see Fig. 9a, b). Here, the sensing performance is analyzed taking $\Omega = 0.9995$ for parametric excitation in the first mode, and $\Omega = 0.995$ for parametric excitation in the second mode. For the excitation in first mode, parameters are $\nu = 0.001, G = 0.001, G_d = 0.0001$, and for the excitation in second mode, parameters are $\nu = 0.002, G = 0.003, G_d = 0.00008$.

To evaluate the performance of the proposed mass sensing scheme, a couple of ways have been chosen. In the first one, a single mass (δm) is considered added on the free end of the cantilever beam. So, the amplitude will shift from A_n^0 to $A_n^{\delta m}$. Here, $n = 1$ and $n = 2$ refers to the first and second modes respectively. The relative change in the amplitude would be $\frac{A_n^{\delta m} - A_n^0}{A_n^0}$. For first and second modes, it is shown in Fig. 10a, b, respectively. Figures show that for a large value of added mass, the change in the amplitude is also large. That is because the shift in the natural frequency increases with some increase in δm .

In the second case, a certain value of mass is added incrementally, and the relative change in amplitude is measured. In this case, the relative change in the amplitude would be $\frac{A_n^{i+1} - A_n^i}{A_n^i}$. Here, A_n^i refers to the amplitude of oscillation after adding the fixed value of mass i times. For the first and second modes, the relative change in amplitude is shown in Fig. 10c, d, respectively. δm on the x-axis is the total mass added at i th iteration. This evaluation gives more insights to extract the best sensing

Table 2 Comparison of the change in amplitude both the excitations in first mode

Excitation gains and damping coefficient	δm	Multiple scales parametric	Direct	Galerkin parametric	Direct
$\nu = 0.001, \Omega = 1$	0	0.138	0.139	0.1344	0.138
	10^{-4}	0.157	0.1461	0.15066	0.1452
		13.76%	5.10%	12.10%	5.21%
$G = 8 \times 10^{-4}$ $G_d = 5.5 \times 10^{-5}$	5×10^{-4}	0.212	0.17	0.2023	0.1707
		53.62%	22.30%	50.52%	23.70%
$\nu = 0.001, \Omega = 0.9995$	0	0.072	0.1469	0.07	0.1472
	5×10^{-4}	0.176	0.1872	0.168	0.1846
		144.40%	27.43%	140%	25.40%
$G = 10^{-3}, G_d = 10^{-4}$	10^{-3}	0.2387	0.2257	0.2254	0.2231
		231.52%	53.64%	222%	51.56%

Table 3 Comparison of the change in amplitude for both the excitations in second mode

Excitation gains and damping coefficient	δm	Perturbation parametric	Direct	Galerkin parametric	Direct
$\nu = 0.002,$ $\Omega = 0.995,$ $G = 0.003,$ $G_d = 8 \times 10^{-5}$	0	0.03	0.0326	0.03017	0.033
	5×10^{-4}	0.0273	0.0305	0.0277	0.0308
		− 9.00%	− 6.80%	− 8.18%	− 6.30%
$G = 0.003,$ $G_d = 8 \times 10^{-5}$	0.0025	0.011	0.0217	0.0114	0.02195
		− 63.33%	− 33.12%	− 62.20%	− 33.28%

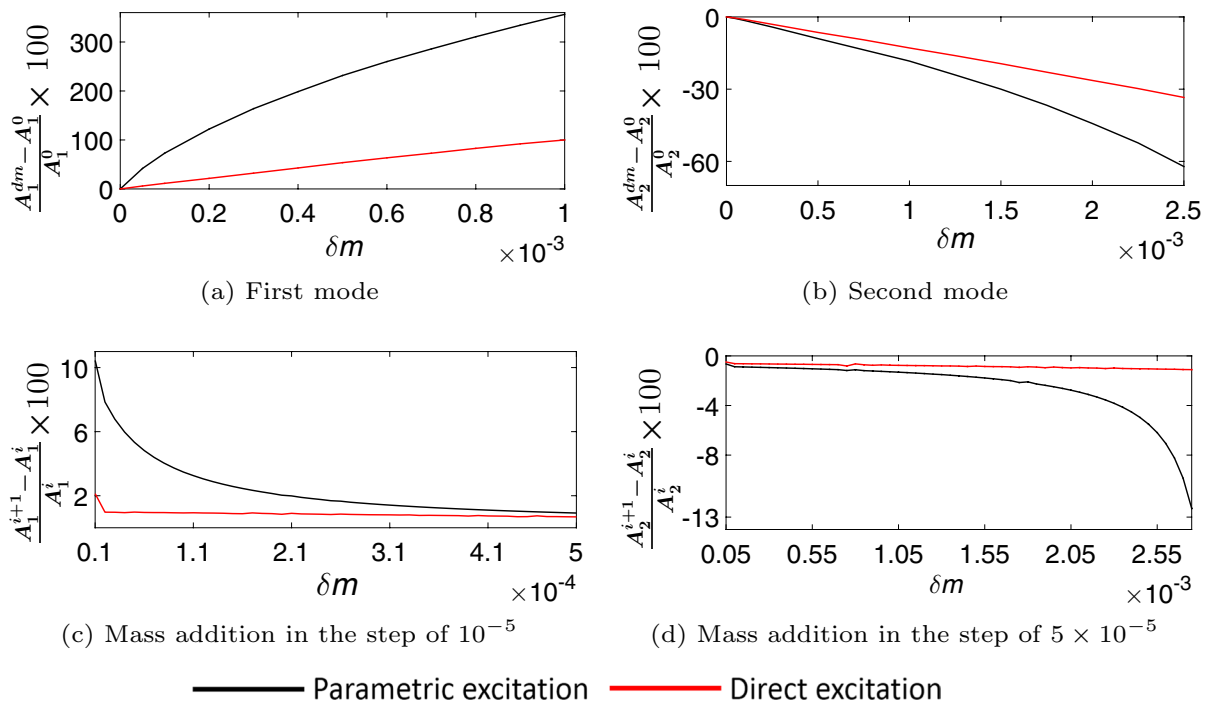


Fig. 10 a, b Relative change in the amplitude due to addition of δm mass, and c, d relative change in the amplitude due to incremental addition of mass, where δm is the total mass added

performance. While evaluating sensing performance for excitation in the first mode, mass is added incrementally in the steps of 10^{-5} , and in the case of excitation in the second mode, the value is 5×10^{-5} . If the steady-state amplitudes before and after addition of mass are within the region where the slope of the amplitude-frequency curve is large, then the relative change in amplitude is also large. That can provide the highest sensitivity. If both the amplitudes are within the region where the slope is small, then the relative variation in amplitude will be nearly equal to that in case of direct excitation. In both the evaluations, parametric excitation based detection is found more sensitive.

Parametric excitation gain (G) and damping coefficient (ν) influence the amplitude variation. When the damping coefficient is large, it is necessary to increase the gain to generate parametric resonance. But, usage of large gain reduces the slope of the amplitude-frequency curve. For example, to examine sensing through excitations in the second mode, the parametric gain and damping coefficient values are intentionally kept larger. That reduces the

relative variation in amplitude. So, a smaller damping coefficient and excitation gain are desirable for best performance. However, the proposed technique can provide good performance in the presence of large damping also. That has been described further.

5.3.2 Sensitivity analysis

Sensitivity of a mass sensor based on shift in the natural frequency has been defined in Chapter 5. One can calculate the value of S^{ω_n} for the nondimensionalized cantilever beam as, $S^{\omega_n} = 2$. For the proposed technique, sensitivity can be defined as

$$S_n = \frac{A_n^{\delta m} - A_n^0}{\delta m} \quad (49)$$

S_1 (S_2) is sensitivity of mass sensor, when parametric excitation is carried out in first (second) mode. S^{ω_n} is a constant value, whereas S_n depends on the value of added mass, and also on the modulation frequency (2Ω).

For several values of added mass δm and modulation frequencies, sensitivity values are plotted as a density plot in Fig. 10c, d, for first mode and second mode, respectively. For second mode based mass detection, gain and damping values are intentionally kept high which results into reduced sensitivity. Using the relationship Eq. (49), sensitivity analysis has been carried out for different values of added mass and modulation frequency. Excitation and damping parameters used for parametric actuation in the first mode are $\nu = 0.001$, $G = 0.001$, and the respective parameters for the actuation in the second mode are $\nu = 0.002$, $G = 0.003$. Results for this analysis are shown in Fig. 11a, b respectively. Value of sensor nonlinearity has been chosen very small, $\alpha = -0.001$. That is desirable for better performance while using amplitude variation based mass detection strategy.

Figures 11a, b provide very important information for mass detection. For modulation frequency (2Ω) chosen in the region of the highest slope, if the added mass value is small, then it provides extremely high sensitivity. For small masses, first mode based detection is better, whereas, for large masses, second mode based detection can give good performance. For sensing of large masses or a large range of mass detection, the parametric instability region should be broad. So, a large gain needs to be used. In that case, the slope of the amplitude-frequency curve decreases, and so sensitivity also decreases.

Certain region in Fig. 11b is blank. Because if the amplitude after mass addition is in the region where only a stable trivial fixed point exists, which is trivial, then sensing is not possible. For parametric excitation in the second mode, only a stable trivial fixed point

exists in region III. In such cases, mass sensing isn't possible, and the sensitivity can't be calculated.

5.3.3 Mass sensing under the effect of large damping

Whenever a microbeam or plate oscillates in the fluidic medium, some additional fluid mass is carried by it. If the microstructure is resonated in the air, then the additional fluid mass is negligible compared to the mass of the beam. However, while carrying out the experiment in the liquid medium, the additional mass is very large. It acts as a loading opposing the motion, which reduces natural frequency also.

Mass sensing is often carried out in the liquid environment to measure chemical and biological particles. Here, the main drawback is very large damping, which reduces the quality factor drastically. Consequently, the sensing performance of resonant MEMS also degrades. Damping coefficient for the excitation of microcantilever beam in a viscous medium can be calculated using the formula [50],

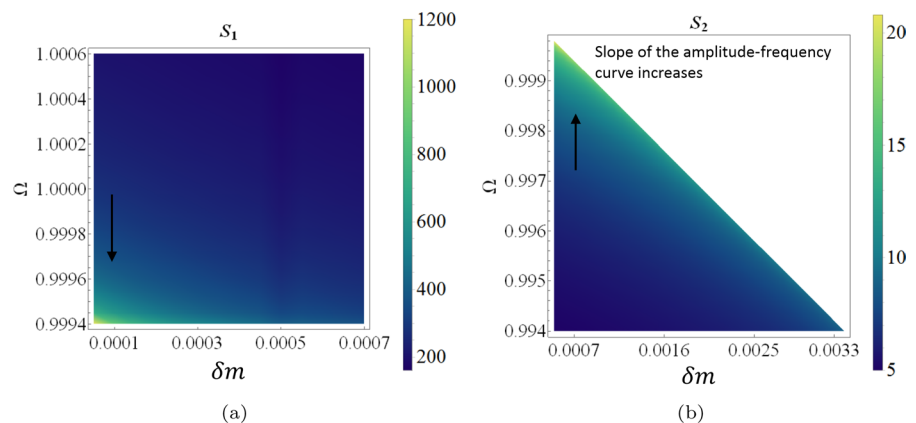
$$C_d = \frac{\pi}{4} \rho_f b^2 \Omega \Gamma'', \quad (50)$$

where ω is the frequency of excitation, and ρ_f is the density of liquid medium. Nondimensionalized damping coefficient can be given as

$$\nu = \frac{\pi \rho_f b^2 \Gamma''}{4 \rho A \left(1 + \frac{\pi \rho_f b \Gamma'}{\rho d} \right)}. \quad (51)$$

Here Γ' and Γ'' are the real and imaginary parts of a hydrodynamic function [7, 50, 51],

Fig. 11 Sensitivity for mass detection based on parametric excitation (a) in the first mode and (b) in the second mode



$$\Gamma = \Gamma' + i\Gamma''.$$

Taking water as a medium, the nondimensionalized damping coefficient is approximated as $\nu = 0.2$, which is extremely large compared to the damping coefficient for air or some other gaseous medium. Here, to generate parametric resonance in the presence of large damping, it is required to use large gain, which reduces the slope of the amplitude-frequency curve in the instability regime. It will reduce the sensitivity also. However, the slope of the amplitude-frequency curve isn't so strongly dependent on the damping coefficient as compared to the dependence of quality-factor ($Q \propto C_d^{-1}$). So, the proposed mass detection technique can provide better performance in the liquid medium than resonant sensing. Calculated sensitivity for mass sensing within liquid regime is shown in Fig. 12. Here, with a reduction in gain, sensitivity can be improved.

5.3.4 Comparison of sensitivity with other mass sensing techniques

The usefulness of the proposed mass detection technique has been examined by comparing the sensitivity values. Outcomes of some of the mass sensing demonstrations are listed in Table 4.

The sensors working on the principle of resonance in microbeam structures are considered. Here, c–c refers to the doubly clamped beam. There are also a few mass sensing techniques mentioned which are proposed or studied using numerical analysis. Here, resonant sensing refers to the mass detection scheme based on natural frequency determination. It is most commonly used for mass

sensing. Size of the most of the microbeam models is below 50 μm . The best performance has been achieved when the beam size is very small, and the experiment is carried out in a vacuum condition. Resonant sensing needs either time-consuming frequency sweeps or PLL (phase-locked loop) based continuous tracking of natural frequency. But the method of detecting the change in amplitude is quite simple. Sensitivity for the considered working model can be calculated from the formula Eq. (49).

$$(S_n)_a = S_n \frac{1}{\rho A} \quad (52)$$

Here damping coefficient and parametric gain values are chosen as $\nu = 0.01$ and $G = 0.01$ respectively. The damping coefficient has been calculated for the microcantilever beam oscillation in the air using the formula Eq. (51). The concept of mass sensing based on the variation in amplitude has been presented before using a nanoscale doubly clamped beam [25]. The approach presented in the thesis utilizes the region of parametric instability. Using this technique, for a comparatively large size cantilever beam, nearly equivalent sensitivity has been achieved. For mass sensing in water also, the performance has been evaluated by taking $\nu = 0.2$ and $G = 0.15$ for parametric excitation in the first mode. It is found that the method can provide good performance in the presence of large damping, too.

Displacement sensing with the atomic-scale resolution has already been demonstrated using the OBDM [57]. So, accurately sensing displacement of microcantilever beam in the range of a few nanometers (10–1000 nm) is certainly possible. Also, the

Fig. 12 Mass sensitivity, when the damping coefficient is very large

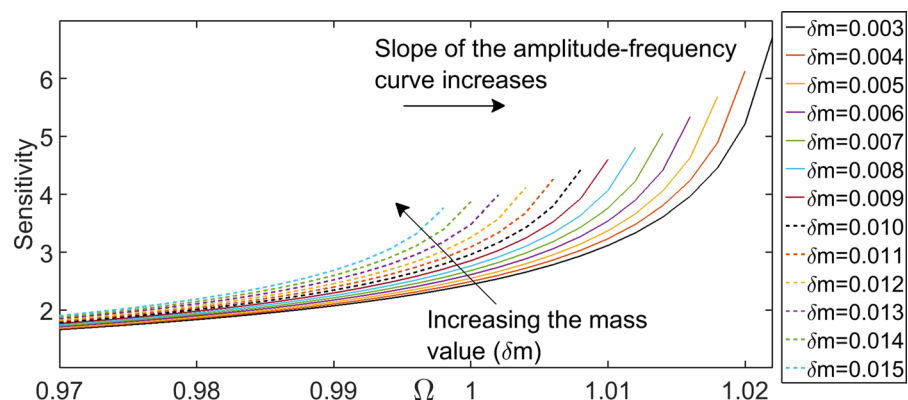


Table 4 Sensitivity data for some of mass sensing techniques

Method of sensing	Microbeam	Length (μm)	Sensitivity
<i>Experimental analysis</i>			
Resonant sensing in vacuum [52]	c-c	12	2 MHz pg^{-1}
Resonant sensing in vacuum [53]	Cantilever	3.5–5	54–194 MHz pg^{-1}
Resonant sensing in vacuum [54]	Cantilever	20–60	0.4–4.6 kHz pg^{-1}
Resonant sensing in air [54]	Cantilever	20–60	0.25–3.15 kHz pg^{-1}
Resonant sensing in vacuum [55]	Cantilever	80	0.8 kHz pg^{-1}
Noise squeezing based sensing [19]	c-c	450	87 Hz/ppb
Bifurcation based sensing [19]	c-c	450	94 Hz/ppb
<i>Numerical analysis</i>			
Resonant sensing [56]	Cantilever	40	0.218 kHz pg^{-1}
Resonant sensing [56]	c-c	40	1.5 kHz pg^{-1}
<i>Numerical analysis based on amplitude change</i>			
Direct excitation [25]	c-c	0.6	0.75 μm pg^{-1}
Parametric excitation, present work	Cantilever	240	4.26 μm pg^{-1}
present work, for sensing in water	Cantilever	240	2.18 μm pg^{-1}

noise squeezing phenomena, which will be discussed in the next chapter, minimizes the influence of noise in detection. So, it is possible to achieve superior performance in mass sensing using the considered working model of the microcantilever beam.

5.3.5 Sensitivity for large values of sensor nonlinearity

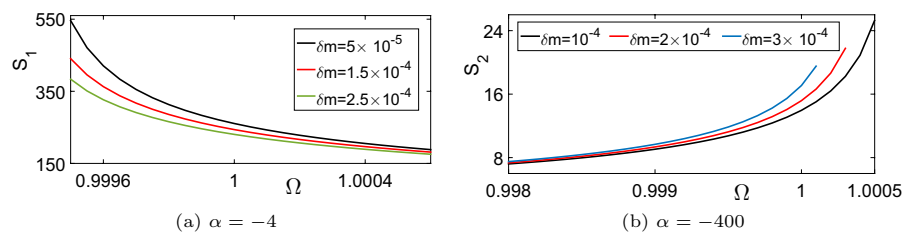
At the beginning of the chapter, it was mentioned that small values of sensor nonlinearity are desirable for the proposed technique. Sometimes the nonlinear characteristics of sensor output are inevitable. Here, the performance of the method is analyzed for large values of α . For parametric excitation in the first mode, sensor nonlinearity is chosen as $\alpha = -4$, and in the case of parametric excitation in the second mode, $\alpha = -400$ is considered. Parametric excitation gain (G) and damping coefficient (ν) values have been

chosen similarly as given in Sect. 5.3.1. Results of multiple scale analysis and numerical simulation are presented in Sect. 5.1. It has been stated before that the slope of the amplitude-frequency curve reduces if the absolute value of α is large. That will also reduce the sensitivity. For few values of δm , sensitivity values are plotted in Fig. 13a, b.

Here, the sensitivity values are found decreased in comparison to results shown in Fig. 11a, b for $\alpha = -0.001$. However, the results show that the proposed technique can certainly provide good sensing performance in the presence of large sensor nonlinearity, too.

5.4 Convergence study

The results of multiple scales technique are validated using numerical methods, namely Galerkin method and GDQM. Considering only one mode in the Galerkin method has been found with satisfactory results.

Fig. 13 Sensitivity for parametric excitation (a) in the first mode and (b) in the second mode for large values of α 

But for large values of α , two-mode approach is necessary to consider the influence of 3Ω harmonics present in the given base displacement with large amplitude. Differential quadrature scheme is a widely used numerical method for nonlinear partial differential equations of motion. In the present study, it provides an excellent match for Ω values close to the natural frequencies, but for other values, the error is large.

The choice of the number of grid points plays a very important in the accuracy of GDQM. For parametric excitation in the first mode (second mode), $N_{DQ} = 6$ ($N_{DQ} = 9$) number of grid points are taken. Choosing a large number of grid points, accuracy can be improved, but the simulation becomes an extremely time consuming process. The total number of terms in the discretized system depends on the different types of nonlinear terms present in the governing equation and also on the number of grid points. For the considered equation, the total number of terms increases with a huge quantity with a unit increase in N_{DQ} . For $N_{DQ} = 6$ ($N_{DQ} = 7$), number of terms are 525(1008), whereas, for $N_{DQ} = 8$ ($N_{DQ} = 9$), number of terms are 1764(2880). So, a large number of grid points makes the simulation extremely difficult. Here, we are mainly interested in the steady-state amplitude within the instability regime, which has been analyzed taking $N_{DQ} = 6$ and $N_{DQ} = 9$ for parametric excitation in the first and second mode, respectively.

A good agreement has been achieved among multiple scales technique, Galerkin method, and GDQM in the regime of parametric instability, whereas, for the Ω values far away from natural frequency error is larger. However, the regime of parametric instability is the region of our interest for the proposed mass sensing strategy.

For some values of N_{DQ} , convergence study of GDQM is carried out. First four natural frequency values for Euler–Bernoulli beam are calculated and shown in Table 5.

Also for parametric excitation in the first and second modes, numerical simulation is carried out for few values of $\Omega \approx \omega_n$, and the outcomes of simulation are shown in Table 6.

In Newmark- β scheme, step size must be much smaller than the minimum time period of the system of equations, i.e. $dt \ll \tau_{N_{DQ}}$. Here, $\tau_{N_{DQ}-1}$ is the time period for the $(N_{DQ} - 1)$ th natural frequency. In addition to that, the modulation of feedback at 2Ω frequency decreases the minimum time period of the system. Consequently, the step size must be very small, if N_{DQ} is large. So, the simulation fails in some cases for large values of N_{DQ} . However, it can be stated that GDQM can be used to approximate the response of the working model. In Table 6, some of the cells are empty which indicates the failure of the simulation or highly inaccurate results.

6 Conclusion

Microcantilever beam with large deflection under feedback-induced parametric excitation is studied using multiple scales and using a couple of numerical methods. The first and second modes are taken into consideration. The influence of geometric and inertial nonlinearities, which appear due to large displacement of the cantilever beam, and the effects of microscale on dynamics have been analyzed. Excellent agreement has been found among the outcomes of perturbation approach and numerical techniques in the region of parametric instability.

Further, a novel mass sensing scheme is proposed that works on the principle of nonlinear parametric resonance in which the region of parametric instability needs to be utilized. Here, it is desirable to minimize the sensor nonlinearity to induce nonlinear parametric resonance through large displacement. Based on the perturbation analysis, performance of the

Table 5 Comparison of natural frequencies approximated through GDQM with analytically obtained values

n	Euler–Bernoulli beam	$N_{DQ} = 5$	$N_{DQ} = 6$	$N_{DQ} = 7$	$N_{DQ} = 8$	$N_{DQ} = 9$
1	1	1.00155	0.999897	0.999995	1	1
2	6.267	6.21288	6.34787	6.25312	6.26429	6.26696
3	17.547	11.4544	15.6673	18.0353	17.3128	17.5082
4	34.386	13.5372	23.978	25.8295	35.8672	32.649

Table 6 Amplitude for different excitation parameters and nonlinearity coefficients for different values of N_{DQ}

1st mode	Ω	Multiple scales	$N_{DQ} = 6$	$N_{DQ} = 7$	$N_{DQ} = 8$	Galerkin 1 mode	Galerkin 2 modes
$\alpha_s=2$	0.999	0.0248	0.033	0.028	0.0264	0.02561	0.0257
$\alpha_i=1$	1	0.0606	0.0655	0.0641	–	0.06101	0.06103
$\alpha_s=8$	1	0.02533	0.02764	0.02641	0.02632	0.025488	0.02547
$\alpha_i=2$	1.001	0.03416	0.0367	0.0362	0.0356	0.03447	0.03445
	1.002	0.04116	0.0425	0.0423	0.0418	0.04152	0.04164
	1.003	0.04727	0.04924	0.0491	–	0.0476	0.0476592
2nd mode	Ω	Multiple scales	$N_{DQ} = 7$	$N_{DQ} = 8$	$N_{DQ} = 9$	Galerkin 1 mode	Galerkin 2 modes
$\alpha_s=1$	0.994	0.032	–	0.028	0.0302	0.0327	–
$\alpha_i=1$	0.996	0.027	–	0.02342	0.025	0.02743	–
	0.998	0.02	–	0.0178	0.01914	0.0209	–

proposed technique is evaluated. It can provide very high sensitivity for mass detection which is comparable to the sensitivity of a nanoscale resonator-based mass sensing. Also, large sensitivity has been noticed for sensing in the liquid medium, where the damping coefficient has a large value. Finally, the convergence of the techniques used for numerical analysis is presented.

Funding No funding was received for conducting this study.

Declarations

Conflict of interest There is no competing interest in publishing the article.

Appendix A: Details of the considered actuation method

The applied base excitation can be stated as given below.

$$w_{\text{base}}(t) = w_{\text{base}}^p(t) + w_{\text{base}}^d(t) \quad (53)$$

Here $w_{\text{base}}^p(t)$ and $w_{\text{base}}^d(t)$ refer to the applied base displacement for solely parametric excitation and direct excitation.

$$w_{\text{base}}^p(t) = 2G(w(L, t) + \alpha_c w(L, t)^3) \cos(2\Omega t) \quad (54a)$$

$$w_{\text{base}}^d(t) = 2G_d \cos(\Omega t) \quad (54b)$$

In this article, the main purpose is to study the dynamics performance of parametric excitation and its usefulness for mass sensing. Direct excitation has been considered just to evaluate the effectiveness of parametric resonance for mass sensing.

For stability analysis and numerical simulation, both the methods of actuation have not been considered simultaneously at any place. However, while using multiple scales approach, both the terms, $w_{\text{base}}^p(t)$ and $w_{\text{base}}^d(t)$ have been considered. For the application of parametric excitation, the given base excitation should be considered as $w_{\text{base}}(t) = w_{\text{base}}^p(t)$, and for the application of direct excitation, it should be taken as $w_{\text{base}}(t) = w_{\text{base}}^d(t)$.

While applying the method of multiple scales, the base excitation has been considered with ϵ^1 order. After choosing ϵ^0 order terms, one will get the equation of motion and boundary conditions for fixed-free cantilever beam. Further, the base excitation will appear into the solvability condition as it has been chosen as of ϵ^1 order.

Appendix B: Analysis of the noise effects

Brief description of the noises present in the considered MEMS resonator is given in Sect. 2. As mentioned before, thermal noise and sensor noise both are white noises. Their effect on the amplitude in the resonance regime has been studied numerically. Here, Galerkin method has been used for the analysis. Influence of thermal forces is determined by considering

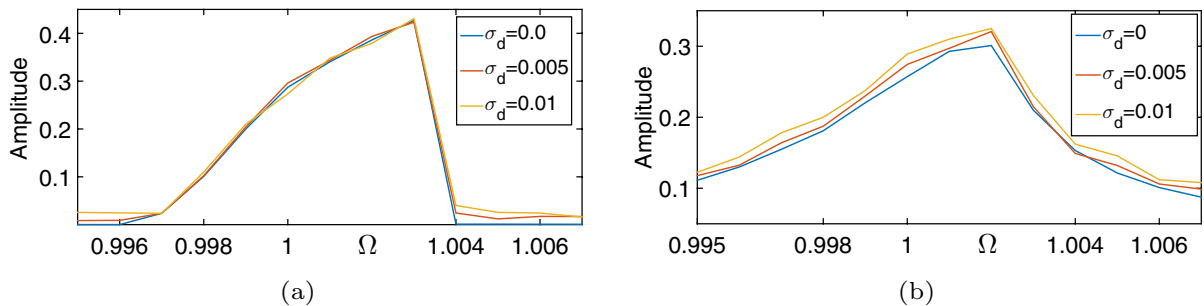


Fig. 14 Amplitude-frequency curve for large deflection of cantilever beam in the presence of noise with different intensities for (a) parametric excitation ($\alpha = -1$), and (based on amplitude change) direct excitation

a random force in the equation of a generalized coordinate derived using Galerkin scheme. One can see Eqs. (47) and (48), where the formulation of Galerkin method is utilized for the microcantilever beam under large deflection. Sensor noise is included within this numerical analysis by adding a random number in the calculated sensor output.

Amplitude-frequency response for parametric and direct excitations is shown in Fig. 14a, b, respectively. Here, σ_d is the standard deviation of the random number considered as the thermal force. Standard deviation of sensor noise is chosen equivalent to $0.1\sigma_d$. Large sensor noise can degrade the performance of feedback-based excitation as it is present in the sensor output and also within the actuation. But detection noise has been found with very small intensity in experimental demonstration of optical beam deflection method [30–32].

The results show that the noises have very less influence on the amplitude in the case of parametric excitation. That will be certainly helpful to determine the amplitude accurately. The mass sensing scheme presented here works on the principle of change in the amplitude. For that purpose, amplitude is needed to be determined with high accuracy. Here, values for excitation gains and damping coefficient are chosen as $G = 0.004$, $G_d = 0.0004$ and $\nu = 0.004$.

References

- Xu X, Melcher J, Raman A (2010) Accurate force spectroscopy in tapping mode atomic force microscopy in liquids. *Phys Rev B*. <https://doi.org/10.1103/physrevb.81.035407>
- Sparks D, Smith R, Cripe J, Schneider R, Najafi N (2003) A portable mems coriolis mass flow sensor. *Sensors* 1:337–339. <https://doi.org/10.1109/icsens.2003.1278953>
- Wang X, Li B, Russo OL, Roman HT, Chin KK, Farmer KR (2006) Diaphragm design guidelines and an optical pressure sensor based on MEMS technique. *Microelectron J* 37(1):50–56. <https://doi.org/10.1016/j.mejo.2005.06.015>
- Jiménez S, Cole MOT, Keogh PS (2016) Vibration sensing in smart machine rotors using internal MEMS accelerometers. *J Sound Vib* 377:58–75. <https://doi.org/10.1016/j.jsv.2016.05.014>
- Ziegler C (2004) Cantilever-based biosensors. *Anal Bioanal Chem* 379(7–8):946–959
- Schmid S, Dohn S, Boisen A (2010) Real-time particle mass spectrometry based on resonant micro strings. *Sensors* 10(9):8092–8100. <https://doi.org/10.3390/s100908092>
- Brand O, Dufour I, Heinrich S, Heinrich SM, Josse F, Fedder GK, Korvink JG, Hierold C, Tabata O (2015) Resonant MEMS: fundamentals, implementation, and application. Wiley, Weinheim. <https://doi.org/10.1002/9783527676330>
- Harne RL, Wang KW (2014) A bifurcation-based coupled linear-bistable system for microscale mass sensing. *J Sound Vib* 333(8):2241–2252. <https://doi.org/10.1016/j.jsv.2013.12.017>
- Turner KL, Burgner CB, Yie Z, Holtoff E (2012) Using nonlinearity to enhance micro/nanosensor performance. *IEEE*. <https://doi.org/10.1109/icsens.2012.6411564>
- Chakraborty G, Jani N (2020) Nonlinear dynamics of resonant microelectromechanical system (MEMS): a review. *Mech Sci*. https://doi.org/10.1007/978-981-15-5712-5_3
- Lifshitz R, Cross MC (2008) Nonlinear dynamics of nanomechanical and micromechanical resonators. *Rev Nonlinear Dyn Complex* 1:1–52. <https://doi.org/10.1002/9783527626359.ch1>
- Mestrom RMC, Fey RHB, Phan KL, Nijmeijer H (2010) Simulations and experiments of hardening and softening resonances in a clamped-clamped beam MEMS resonator. *Sens Actuators A* 162(2):225–234. <https://doi.org/10.1016/j.sna.2010.04.020>
- Delnavaz A, Mahmoodi SN, Jalili N, Ahadian MM, Zohoor H (2009) Nonlinear vibrations of microcantilevers

- subjected to tip-sample interactions: theory and experiment. *J Appl Phys* 106(11):113510. <https://doi.org/10.1063/1.3266000>
14. Rhoads JF, Shaw SW, Turner KL (2009) Nonlinear dynamics and its applications in micro-and nanoresonators. In: ASME 2008 Dynamic systems and control conference, pp. 1509–1538. <https://doi.org/10.1115/dscc2008-2406>. American Society of Mechanical Engineers Digital Collection
 15. Moran K, Burgner C, Shaw S, Turner K (2013) A review of parametric resonance in microelectromechanical systems. *Nonlinear Theory Appl* 4(3):198–224. <https://doi.org/10.1587/nolta.4.198>
 16. Nitzan SH, Zega V, Li M, Ahn CH, Corigliano A, Kenny TW, Horsley DA (2015) Self-induced parametric amplification arising from nonlinear elastic coupling in a micro-mechanical resonating disk gyroscope. *Sci Rep* 5(1):9036. <https://doi.org/10.1038/srep09036>
 17. Linzon Y, Ilic B, Lulinsky S, Krylov S (2013) Efficient parametric excitation of silicon-on-insulator microcantilever beams by fringing electrostatic fields. *J Appl Phys* 113(16):163508. <https://doi.org/10.1063/1.4802680>
 18. Thomas O, Mathieu F, Mansfield W, Huang C, Trolier-McKinstry S, Nicu L (2013) Efficient parametric amplification in micro-resonators with integrated piezoelectric actuation and sensing capabilities. *Appl Phys Lett* 102(16):163504. <https://doi.org/10.1063/1.4802786>
 19. Li LL, Holthoff EL, Shaw LA, Burgner CB, Turner KL (2014) Noise squeezing controlled parametric bifurcation tracking of MIP-coated microbeam MEMS sensor for TNT explosive gas sensing. *J Microelectromech Syst* 23(5):1228–1236. <https://doi.org/10.1109/jmems.2014.2310206>
 20. Yie Z, Miller NJ, Shaw SW, Turner KL (2012) Parametric amplification in a resonant sensing array. *J Micromech Microeng* 22(3):035004. <https://doi.org/10.1088/0960-1317/22/3/035004>
 21. Prakash G, Raman A, Rhoads J, Reifengerger RG (2012) Parametric noise squeezing and parametric resonance of microcantilevers in air and liquid environments. *Rev Sci Instrum* 83(6):065109. <https://doi.org/10.1063/1.4721282>
 22. Moreno-Moreno M, Raman A, Gomez-Herrero J, Reifengerger R (2006) Parametric resonance based scanning probe microscopy. *Appl Phys Lett* 88(19):193108. <https://doi.org/10.1063/1.2202132>
 23. Jani N, Chakraborty G (2020) Parametric resonance in cantilever beam with feedback-induced base excitation. *J Vib Eng Technol* 9(2):291–301. <https://doi.org/10.1007/s42417-020-00226-1>
 24. Jani N, Chakraborty G (2021) Feedback based parametric actuation with sensor nonlinearity and mass sensing. *J Vib Eng Technol*. <https://doi.org/10.1007/s42417-021-00317-7>
 25. Potekin R, Kim S, McFarland DM, Bergman LA, Cho H, Vakakis AF (2018) A micromechanical mass sensing method based on amplitude tracking within an ultra-wide broadband resonance. *Nonlinear Dyn* 92(2):287–304. <https://doi.org/10.1007/s11071-018-4055-y>
 26. Kong S, Zhou S, Nie Z, Wang K (2008) The size-dependent natural frequency of bernoulli-euler micro-beams. *Int J Eng Sci* 46(5):427–437
 27. Rahaeifard M, Kahrobaiyan M, Asghari M, Ahmadian M (2011) Static pull-in analysis of microcantilevers based on the modified couple stress theory. *Sens Actuators A* 171(2):370–374. <https://doi.org/10.1016/j.sna.2011.08.025>
 28. Herfst RW, Klop WA, Eschen M, van den Dool TC, Koster NB, Sadeghian H (2014) Systematic characterization of optical beam deflection measurement system for micro and nanomechanical systems. *Measurement* 56:104–116. <https://doi.org/10.1016/j.measurement.2014.06.016>
 29. Thormann E, Pettersson T, Claesson PM (2009) How to measure forces with atomic force microscopy without significant influence from nonlinear optical lever sensitivity. *Rev Sci Instrum* 80(9):093701. <https://doi.org/10.1063/1.3194048>
 30. Fukuma T, Kimura M, Kobayashi K, Matsushige K, Yamada H (2005) Development of low noise cantilever deflection sensor for multienvironment frequency-modulation atomic force microscopy. *Rev Sci Instrum* 76(5):053704. <https://doi.org/10.1063/1.1896938>
 31. Lübke J, Temmen M, Rode S, Rahe P, Kühnle A, Reichling M (2013) Thermal noise limit for ultra-high vacuum noncontact atomic force microscopy. *Beilstein J Nanotechnol* 4:32–44. <https://doi.org/10.3762/bjnano.4.4>
 32. Lübke J, Temmen M, Rahe P, Kühnle A, Reichling M (2013) Determining cantilever stiffness from thermal noise. *Beilstein J Nanotechnol* 4(1):227–233. <https://doi.org/10.3762/bjnano.4.23>
 33. Piyush P, Jayanth GR (2016) An out-of-plane linear motion measurement system based on optical beam deflection. *Meas Sci Technol* 27(2):025203. <https://doi.org/10.1088/0957-0233/27/2/025203>
 34. Khorshidi MA (2018) The material length scale parameter used in couple stress theories is not a material constant. *Int J Eng Sci* 133:15–25. <https://doi.org/10.1016/j.ijengsci.2018.08.005>
 35. Park SK, Gao X-L (2006) Bernoulli-euler beam model based on a modified couple stress theory. *J Micromech Microeng* 16(11):2355–2359. <https://doi.org/10.1088/0960-1317/16/11/015>
 36. Ma H, Gao X, Reddy J (2008) A microstructure-dependent timoshenko beam model based on a modified couple stress theory. *J Mech Phys Solids* 56(12):3379–3391. <https://doi.org/10.1016/j.jmps.2008.09.007>
 37. Rahi A (2021) Vibration analysis of multiple-layer microbeams based on the modified couple stress theory: analytical approach. *Arch Appl Mech* 91(1):23–32. <https://doi.org/10.1007/s00419-020-01795-z>
 38. Farokhi H, Ghayesh MH, Hussain S (2016) Large-amplitude dynamical behaviour of microcantilevers. *Int J Eng Sci* 106:29–41. <https://doi.org/10.1016/j.ijengsci.2016.03.002>
 39. Li Z, He Y, Zhang B, Lei J, Guo S, Liu D (2019) Experimental investigation and theoretical modelling on nonlinear dynamics of cantilevered microbeams. *Eur J Mech A Solids* 78:103834. <https://doi.org/10.1016/j.euromechsol.2019.103834>
 40. Krenk S (2009) Non-linear modeling and analysis of solids and structures. Cambridge University Press, Cambridge. <https://doi.org/10.1017/cbo9780511812163>

41. Bert CW, Malik M (1996) Differential quadrature method in computational mechanics: a review. *Appl Mech Rev* 49(1):1–28. <https://doi.org/10.1115/1.3101882>
42. Karami G, Malekzadeh P (2002) A new differential quadrature methodology for beam analysis and the associated differential quadrature element method. *Comput Methods Appl Mech Eng* 191(32):3509–3526. [https://doi.org/10.1016/s0045-7825\(02\)00289-x](https://doi.org/10.1016/s0045-7825(02)00289-x)
43. Du H, Lim MK, Lin RM (1994) Application of generalized differential quadrature method to structural problems. *Int J Numer Meth Eng* 37(11):1881–1896. <https://doi.org/10.1002/nme.1620371107>
44. Mao X-Y, Sun J-Q, Ding H, Chen L-Q (2020) An approximate method for one-dimensional structures with strong nonlinear and nonhomogenous boundary conditions. *J Sound Vib* 469:115128. <https://doi.org/10.1016/j.jsv.2019.115128>
45. Shu C (2000) *Differential quadrature and its application in engineering*. Springer, London. <https://doi.org/10.1007/978-1-4471-0407-0>
46. Sadeghian H, Rezazadeh G, Osterberg PM (2007) Application of the generalized differential quadrature method to the study of pull-in phenomena of MEMS switches. *J Microelectromech Syst* 16(6):1334–1340. <https://doi.org/10.1109/jmems.2007.909237>
47. Sassi SB, Najari F (2018) Strong nonlinear dynamics of MEMS and NEMS structures based on semi-analytical approaches. *Commun Nonlinear Sci Numer Simul* 61:1–21. <https://doi.org/10.1016/j.cnsns.2018.01.022>
48. Nayfeh AH, Pai PF (2004) *Linear and nonlinear structural mechanics*. Wiley, Weinheim. <https://doi.org/10.1002/9783527617562>
49. Yang YT, Callegari C, Feng XL, Ekinici KL, Roukes ML (2006) Zeptogram-scale nanomechanical mass sensing. *Nano Lett* 6(4):583–586. <https://doi.org/10.1021/nl052134m>
50. Maali A, Hurth C, Boisgard R, Jai C, Cohen-Bouhacina T, Aimé J-P (2005) Hydrodynamics of oscillating atomic force microscopy cantilevers in viscous fluids. *J Appl Phys* 97(7):074907. <https://doi.org/10.1063/1.1873060>
51. Sader JE (1998) Frequency response of cantilever beams immersed in viscous fluids with applications to the atomic force microscope. *J Appl Phys* 84(1):64–76. <https://doi.org/10.1063/1.368002>
52. Baek I-B, Byun S, Lee BK, Ryu J-H, Kim Y, Yoon YS, Jang WI, Lee S, Yu HY (2017) Attogram mass sensing based on silicon microbeam resonators. *Sci Rep* 7(1):1–10. <https://doi.org/10.1038/srep46660>
53. Ilic B, Yang Y, Aubin K, Reichenbach R, Krylov S, Craighead HG (2005) Enumeration of DNA molecules bound to a nanomechanical oscillator. *Nano Lett* 5(5):925–929. <https://doi.org/10.1021/nl050456k>
54. Pinto RMR, Brito P, Chu V, Conde JP (2019) Thin-film silicon MEMS for dynamic mass sensing in vacuum and air: Phase noise, allan deviation, mass sensitivity and limits of detection. *J Microelectromech Syst* 28(3):390–400. <https://doi.org/10.1109/jmems.2019.2911666>
55. Chen Z, Zhao F (2014) Single crystalline 4h-polytype silicon carbide microresonator sensor for mass detection. *Mater Lett* 128:64–67. <https://doi.org/10.1016/j.matlet.2014.04.093>
56. Nathani MU, Nazemi H, Love C, Lopez YB, Swaminathan S, Emadi A (2020) Capacitive based micromachined resonators for low level mass detection. *Micromachines* 12(1):13. <https://doi.org/10.3390/mi12010013>
57. Putman CAJ, Grooth BGD, Hulst NFV, Greve J (1992) A detailed analysis of the optical beam deflection technique for use in atomic force microscopy. *J Appl Phys* 72(1):6–12. <https://doi.org/10.1063/1.352149>

Publisher's Note Springer Nature remains neutral with regard to jurisdictional claims in published maps and institutional affiliations.

Springer Nature or its licensor (e.g. a society or other partner) holds exclusive rights to this article under a publishing agreement with the author(s) or other rightsholder(s); author self-archiving of the accepted manuscript version of this article is solely governed by the terms of such publishing agreement and applicable law.